# Synthetic Routes to Hybrid Nanoparticles of Gold and Copper Sulfides

By

Summer Laurel Arrowood

Thesis

Submitted to the Faculty of the

Graduate School of Vanderbilt University

in partial fulfillment of the requirements

for the degree of

MASTER OF SCIENCE

in

Chemistry

May, 2016

Nashville, Tennessee

Approved:

Janet E. Macdonald, Ph.D.

David Cliffel, Ph.D.

To my parents and sister, for their unending support

and

To my cat, Red, and dog, Opie, for their existence

## ACKNOWLEDGEMENTS

This project was possible with the support of funding from the Vanderbilt University Department of Chemistry, a Vanderbilt Discovery grant, TN-Score, and the D. Stanley and Ann T. Tarbell Endowment Fund.

There are a number of extremely talented scientists who guided me on my journey. My advisor, Dr. Janet Macdonald, collaborators Dr. Richard Haglund and Roderick Davidson, and all the members of my committee have truly pushed me to be the best scientist I can be. Additionally I would like to thank my lab mates for their professional feedback and emotional support.

Finally, without the continuous support and sacrifices of my parents and the unrelenting encouragement of my sister, none of this would have ever been possible.

## TABLE OF CONTENTS

Page

## LIST OF FIGURES

# CHAPTER I

## GENERAL INTRODUCTION

Nanoparticles (NPs), particles of material at the dimension of <100 nm, offer a way to access and control properties not observed in bulk materials or molecular species. This is due to confinement effects (quantum and dielectric) and the enormous increase of surface area-to-volume ratio relative to bulk materials.[1] Properties such as optical absorption, optical emission, reactivity, and catalytic activity can be altered through changing particle size and morphology. This control of material properties is a useful tool for exploring how nanoparticles interact with the environment and each other.

Semiconductor nanoparticles have size-tunable band gaps and high quantum yield. For these reasons, they are often studied for light-absorption and emission applications, including solar energy collection, theranostics, and LEDs.[2] Metal nanoparticles likewise show size-dependent properties at the nanoscale, such as localized surface plasmon resonance(LSPR) and increased catalytic activity.[3] Since size and shape are intrinsically linked to optoelectronic properties, developing and improving synthetic methods to better control nanoparticle morphology is crucial to both understanding this relationship and facilitating particle applications.

Colloidal synthesis supplies sophisticated control over the size, shape, and composition of the nanoparticle product.[2,3] It is an efficient way to obtain relatively large quantities of monodisperse particles. A variety of factors can be manipulated to control the resulting particles, including precursor type, reaction time and temperature, injections, surfactants, and even stir rate.

The unique control over properties at the nanoscale can be augmented by the addition of other nanoscale components to the original particle[4]. These constructs, comprised of two or more

nanomaterials in a single particle, are known as hybrid nanoparticles. In the design of a hybrid system, a second material domain can serve many purposes,[1,5,6] contributing its own functionality to the whole or coupling with the other domain to dramatically change existing properties and synergistically create a whole with markedly different properties than either component. Some recent examples include facilitating charge separation within a catalytic nanoparticle by adding a metal domain, adding a silica shell to render gold nanoparticles stable in solution and easily functionalizable, and passivating the surface of semiconductor nanoparticles with a wider-band-gap material to improvement confinement and quantum yield.[7–9]

Hybrid nanoparticles are often created by first making a 'seed' particle of an initial material, and adding another domain *via* a second growth step that is nucleated on the seed particles. The way this secondary growth step manifests depends greatly upon the materials being hybridized, but the major patterns of growth seen in this report can be simplified to core-shell type growth or the formation of dimers *via* nucleation of a new domain onto a single point such as a specific crystal face, edge, or vertex.[4,6,10]

There are inherent synthetic challenges in the controlled creation of nanoparticles combining two disparate materials, such as the proposed Au—CuS hybrid. When working with two crystalline materials, the lattice constant mismatch must be minimalized for heterogeneous nucleation of the second material to occur. The synthetic conditions must be compatible with both materials, both to ensure dispersibility (for solution-phase syntheses) and to avoid the destruction of the seed domain. Surface characteristics of the materials must be considered, such as the composition of facets, the presence of surface defects, and interfacial energy between the materials. Miscibility of the materials and precursors must also be considered.

In this work, the synthesis of various hybrid nanoparticles of gold, gold and copper sulfides, and silica is explored. In the first portion of this work, dual-plasmonic gold-copper sulfide nanoparticles are synthesized and their nonlinear optical properties briefly investigated. In the second portion of this work, copper sulfide nanoplatelets are used as a template material in a cation exchange reaction to create gold sulfide nanoparticles, and hybrid nanoparticles of gold sulfide and copper sulfide.

# CHAPTER II

## DESIGN AND SYNTHESIS OF A DUAL-PLASMONIC HYBRID NANOPARTICLE SYSTEM

Many hybrid nanoparticle designs pair a metal domain with a semiconductor domain.[11,12] Metallic nanomaterials, especially those of noble metals, are highly influential in hybrid systems in part due to the localized surface plasmon resonances (LSPRs) exhibited by these materials at the nanoscale.[1] LSPRs result from the collective oscillation of surface charges on nanoparticles in response to specific frequencies of incident light(Figure 1). Metallic nanoparticles often have LSPRs in the visible to near-UV range,[13–15] and many semiconductor nanoparticles can be doped to manifest LSPRs in the near IR.[16–21] The surface and immediate surroundings of a nanoparticle with an excited LSPR are considered an electric field 'hotspot.'[22] This enormous electric field enhancement has far-reaching implications when a component exhibiting LSPR is incorporated into a hybrid nanoparticle,[14,23–25] such as enhanced catalytic properties and absorption of light, carrier transfer enhanced excitation or decay, and so forth.[1,26,27] The use of one or more domains exhibiting LSPR in a hybrid nanoparticle can result in astonishing new material properties.

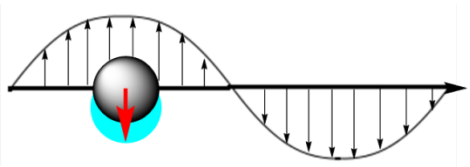

**Figure 1** Simplified scheme of charges on a nanoparticle interacting with the electric field of light, forming an LSPR.

The property this project hopes to enhance via LSPR is a nonlinear optical effect[28–30] known as second harmonic generation (SHG), which is a special case of sum frequency generation. In this project, we hope to use hybrid systems to demonstrate enhanced SHG by using LSPRs to enhance the electric fields at both the fundamental and second harmonic frequencies. This sort of enhancement of SHG by nanoparticle dimer systems has some literature

precedent.[31–35] However, there are no known published instances of a heterodimer nanoparticle system with two resonant LSPRs resulting in enhancement of SHG.

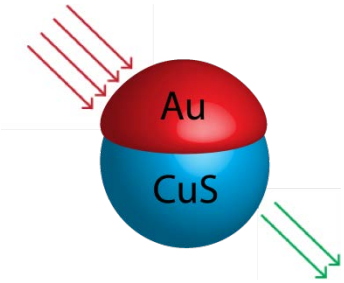

**Figure 2** General hybrid scheme

In this nanoparticle system (Figure 2), a gold nanoparticle is paired with a semiconductor NP in order to enhance SHG via the combined LSPR field effects of the two domains. In its simplest spherical form, nano-gold has a pronounced LSPR at around 530 nm. Many copper chalcogenides, such as $Cu_2Se$ (the first semiconductor applied to this project), can be oxidized to exhibit hole-based LSPR in the near-IR spectral region.[36] However, the copper chalcogenide used for most of the work reported here, copper sulfide (CuS, covellite), [37,38] derives its LSPR from inherent features of its crystal structure. The copper oxidation state in covellite is +1, with the extra hole necessary for charge balance delocalized into the sulfur-sulfur bonds.[39,40] The result is a stoichiometric quantity of delocalized holes in the material, which causes a very strong and sharp LSPR peak centered at close to 1100 nm. These CuS NPs are also reasonably resistant to degradation under normal atmospheric conditions, and the strength of the LSPR makes them a desirable alternative to other copper chalcogenides in the hybrid system. Additionally, there is a pronounced absorption minimum at 520-550 nm, ensuring that reabsorption by the semiconductor band gap of any SHG generated will be minimized, which was a concern with copper selenide nanoparticles. If enhancement of SHG is achieved using this dual LSPR system, the insight into NP-NP LSPR dynamics could pave the way to advances in microscopy, optics, sensing, and related fields. Although there are many reports on metal-metal hybrids with dual plasmons[41,42], there are few reports of metal-semiconductor systems with two LSPR resonances.[43,44] Furthermore, the insights into the creation of hybrid nanomaterials with plasmonic enhancement over an

extremely broad spectral region has further value in areas including photothermal therapy, photoabsorbers, and catalysis. The colloidal synthesis of a hybrid system containing two LSPRs for possible SHG enhancement comprises the first portion of this work.

## Synthesis of gold-copper selenide hybrids

Initial efforts in this project used oxidized copper selenide ($Cu_{2-x}Se$) NPs as the source of the NIR LSPR for the hybrid system. This material has a very broad LSPR peak that extends through a large portion of the NIR. Furthermore, once the surface of the nanoparticles has oxidized to a certain point, the NPs are in the more stable $Cu_{1.8}Se$ form[18] that resists further oxidation and degradation under normal conditions. The first design was to simply grow a gold domain onto a $Cu_{2-x}Se$ nanoparticle following a literature procedure for growing gold on CdSe dots and nanorods.[45] (Complete synthetic detail is presented in Appendix I.) The TEM showed this route resulted in a heterodimer with a distinct $Cu_2Se$ domain and an Au domain that was apparent as a high-contrast domain on the copper selenide particles in TEM images. The Au domain was also seen as an LSPR peak at around 520 nm in the UV-Vis spectrum. (Figure 3) However, if the gold domain was grown on a $Cu_{2-x}Se$ particle that had not experienced any surface oxidation (*i.e.*, no LSPR peak in the IR absorption), the appearance of a NIR LSPR could not be induced post hybridization, whether through exposing the particles to atmospheric oxygen and water or through the addition of oxidizing agents such as ceric ammonium nitrate, both of which were more than sufficient to induce LSPRs in unaltered $Cu_2Se$ NPs. If an Au domain was grown on

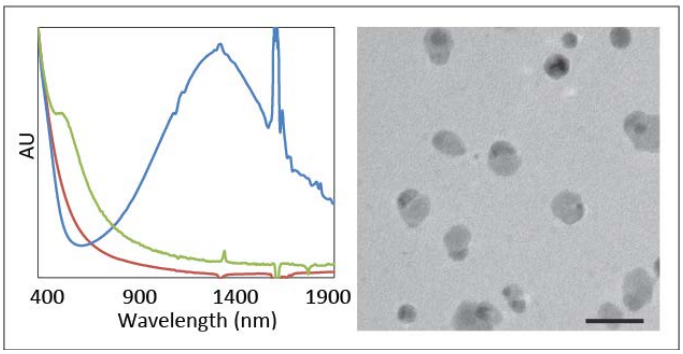


**Figure 3** a) UV-Vis for $Cu_2Se$ (red), $Cu_{2-x}Se$ (blue), and Au-$Cu_{2-x}Se$ (green). b) TEM image of hybrid particles (scale bar=20 nm**)**

pre-oxidized $Cu_{2-x}Se$ nanoparticles, the NIR LSPR disappeared entirely, and the Au LSPR that appeared was much less intense and red-shifted compared to the Au LSPR on unoxidized $Cu_2Se$. The red-shift of the Au LSPR can be an indication of decreased charge carrier density at the Au domain. The conclusion was reached that an Au monolayer must be forming in addition to the larger Au domains, and/or copper vacancies were being filled by gold, which resulted in the quench of the NIR LSPR. This hypothesis could have been confirmed with STEM-EDS mapping, but at the time of this work this capability was not available.

Some months after the direct hybrid synthesis was completed, a paper was published for a similar Au-$Cu_{2-x}Se$ hybrid NP system that observed the same quenching/shifting trends,[44] though LSPR quenching was not as complete for their hybrids as it was for the hybrids synthesized in this project. In this example, the quench and shift of LSPRs was attributed to charge transfer between the two domains, hole diffusion from the $Cu_{2-x}Se$ to the Au being sufficient to significantly reduce the carrier density of both domains. Further shift of the LSPRs than could be attributed to reduced carrier density was explained as due to the change of the dielectric constant surrounding each domain with the formation of the hybrid. This was also a reasonable explanation for both the loss of NIR LSPR and the reduction of the Au LSPR in the direct hybrid system synthesized here.

Since direct growth of domains did not preserve LSPRs, the conclusion was reached that the domains needed to be separated chemically and electronically. The most straightforward way to achieve this separation was to place a dielectric barrier on one of the material domains, and to attach the other domain to that barrier.

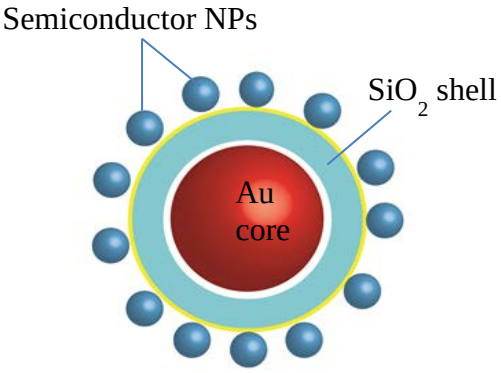


**Figure 4** Hybrid scheme with silica shell, cross-sectional view.

A number of strategies could be implemented to create a barrier between the two domains, such as using a long-chain bifunctional linker molecule, adding a polymer shell, *etc*.[46–48] Of these strategies, placing a silica shell between the gold and semiconductor domains was selected as the best solution, as inspired by many literature examples[49–52]. The silica shelling of many different types of nanoparticles is widely studied due to the several material advantages offered; $SiO_2$ is transparent in the regions of interest for this project, it is very resistant to degradation, and it is synthetically convenient for the materials used in this hybrid scheme. Once completely shelled, Au@$SiO_2$ NPs are resilient, and the shells do not degrade or transform under the electron beam of the TEM so shell thickness can be accurately measured. These accurate measurements will allow the study of interparticle distance effects on LSPR enhancement. From a synthetic standpoint, an $SiO_2$ surface can easily be functionalized through basic sol-gel chemistry, allowing attachment of almost any conceivable functionality.[49] Furthermore, many standard Au NP syntheses are aqueous, and as $SiO_2$ sol-gel shelling chemistry usually requires a polar solvent,[53–55] the shelling synthesis is compatible with the Au NPs.

**Gold nanoparticle synthesis and silica shelling**

A sodium citrate reduction[56] of chloroauric acid ($HAuCl_4$) was used to synthesize 16 nm spherical Au NPs with an LSPR at a wavelength of 520 nm. For the research presented here, this synthesis is superior to the other commonly seen Au NP syntheses[24,25,57] because there are fewer excess surfactants present and the product typically has higher monodispersity and few to no irregular (non-spherical) components. The nanoparticles are supported in aqueous solution by the citrate ions that cap the surface.

The citrate-capped Au NPs offered a surface on which a very thin silica shell can be deposited. Keeping distances between Au and CuS very small was important to ensure plasmonic

interaction. Most literature $SiO_2$ shelling procedures[49,58] (usually using the Stöber method) result in shells that are too thick for the purposes of this project.[50] These Stöber shells are on the order of 50-100 nm, past the size regime (within 20 nm) at which LSPR interaction is expected to occur for 16 nm NPs.[59] It was possible to manipulate a combination of literature $SiO_2$ shelling procedures[8,60] to tune shell thickness of batches anywhere from 4-17 nm. In this process, the first step was to displace the citrate capping layer with 3-aminopropyltrimethoxysilane (APTES). The amines adhere to the Au surface, leaving Si-O-R terminating groups facing outwards and rendering the surface vitreophilic. The terminal alkoxy groups provide a nucleation point for the condensation of $SiO_2$ shells from addition of a sodium silicate solution. Condensation of the silica shells from the sodium silicate solution was driven by decreasing the pH of the solution. After 7+ days of gentle stirring, a 2-4 nm silica shell formed on the Au NPs. Shell growth was monitored via TEM. This shell was terminated with hydroxyl groups that provide an ideal platform for further shell growth *via* a sol-gel type technique. Addition of a solution of tetraethylorthosilicate (TEOS) and ammonium hydroxide resulted in a base-catalyzed hydrolysis

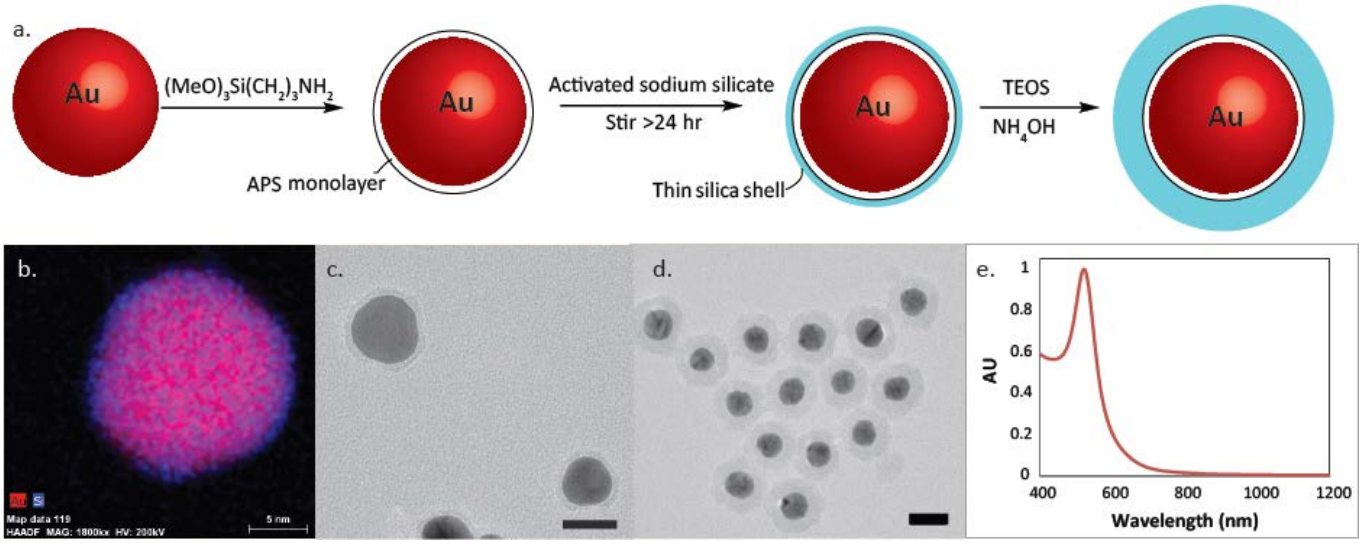


**Figure 5** a) Silica shelling scheme. b) STEM-EDS elemental map of Au NP after silicate addition. c) and d) Two different shell thicknesses achieved by adding different quantities of TEOS. e) UV-Vis showing preservation of LSPR (Scale bars=20nm)

polymerization to slowly build thicker shell onto the Au@$SiO_2$. Final thickness of the shell was largely controlled by reaction time, typically running anywhere from a few days to a few weeks (depending on desired shell thickness, with longer times typically resulting in thicker shells) of gentle stirring in ambient conditions. Progress of shell growth was monitored via TEM. After this final shell addition step, $SiO_2$ shell thickness ranged from 5 to 17 or more nanometers with a typical standard deviation of 1.5 nm per batch.

**Silica shell functionalization**

Next, the shells were functionalized with 3-(trimethoxysilyl)propyl methacrylate (TPM). TPM functionalization was necessary for transfer to nonpolar solvent, long-term particle stability, and compatibility with the copper sulfide domain. Au@$SiO_2$ without a stabilizing group irreversibly aggregates with time, usually on the scale of weeks to months. In order to achieve both nonpolar solubility and surface stability of the Au@$SiO_2$, a literature procedure[49] was modified to add a methacrylate functionality to the silica surface after the desired shell thickness was achieved. In short, the Au@$SiO_2$ solution was refluxed with ethanol and TPM until the particles readily transferred from the $H_2O$/EtOH mixture to a $CHCl_3$/EtOH solvent mixture. Once this functionalization was achieved, the particles could be concentrated and stored for extended periods of time without any change in optical properties or agglomeration.

The final functionalization necessary was the addition of an amine so that copper chalcogenide nanoparticles would adhere to the $SiO_2$ surface. The CuS used in this synthesis is passivated with oleylamine, so an amine is reasonably expected to displace the labile oleylamine and adhere to the surface of CuS. 3-aminopropyltrimethoxy silane (APTES) is a readily available reagent and there is ample literature precedent for its use in adding an amine functionality to silica surfaces.[8,49,61] Altering and combining these precedents resulted in a successful

functionalization through stirring the TPM-functionalized $Au@SiO_2$ in a solution of APTES and EtOH for sixteen hours followed by reflux. The reflux steps were repeated until functionalization occurred as evinced by the attachment of CuS NPs when tested.

Preparation of the hybrids was accomplished by the addition of a solution of CuS NPs (synthetic details in Appendix A) to the functionalized $Au@SiO_2$ in tetrahydrofuran (THF) followed by stirring for thirty minutes. This formed hybrid superstructures (TEM images in supplementary information), in which the adherence of CuS to multiple $SiO_2$ surface resulted in agglomeration of both types of particles on the microscale. Typically, $Au@SiO_2$ cores were covered in CuS platelets. Due to the large size of these hybrid superstructures, they were easily recovered via centrifugation, while unattached CuS remained in solution.

## Testing for SHG

To test nanoparticles for SHG, it was decided that depositing the particles as a film on a glass slide, as opposed to a liquid suspension, would yield the most robust samples and be most applicable to the available analytical setup, especially as the superstructures eventually settled out of solution due to their large size. Initial trial tests for SHG on controls demonstrated the necessity of high optical density samples, so the preparation of very thick, even films was essential for quantifiable measurements. These requirements are difficult to meet *via* standard film-preparation procedures such as drop-casting or spin-coating. To overcome this difficulty, the sample mount substrate, fluorine-doped tin oxide (FTO)-coated glass, was cut so it fit into a 6-dram glass vial. The mount

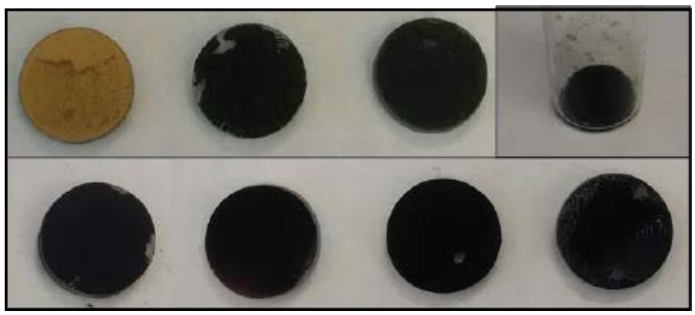

**Figure 6** Clockwise from top left: Gold and copper sulfide blanks and direct hybrids; a 6-dram vial containing a freshly prepared film, and all three core-shell hybrids and the covellite CuS sample.

was placed in the bottom of the glass vial, and the vial was then filled with a nanoparticle suspension and centrifuged so that a film of nanoparticles was deposited onto the mount, which was then air-dried and stored under vacuum in a desiccator. This yielded films with a thickness and composition that was easily controlled by altering the contents and concentration of the NP solution.

The samples and controls that were prepared for SHG analysis are listed in the table below. In addition to the Au@$SiO_2$-CuS hybrid structures, a recent literature example[43] of direct Au-$Cu_{2-x}S$ hybrids were tested for SHG. (Figure 7) These hybrids consisted of a 10 nm gold core particle surrounded by a "Saturn-like" disk of copper sulfide. They differ dramatically from the other direct gold-copper chalcogenide hybrids mentioned[44] in that they demonstrate plasmonic *enhancement* in both LSPRs, which the authors hypothesized as being due to electron transfer from the copper sulfide to the gold core, which increased charge carrier density in both domains. This is in direct contrast to the $Cu_2Se$-Au heterodimers originally synthesized in this project, where the LSPR of both domains was quenched in the hybrid nanoparticle.

| Sample # | Contents |
|---|---|
| 1 | 10 nm Au NPs, Jiang control |
| 2 | Copper Sulfide NPs Jiang control |
| 3 | Direct hybrids (Jiang) Au-CuS |
| 4 | Covellite CuS NPs |
| 5 | 4 nm shells Au@$SiO_2$--CuS |
| 6 | 17 nm shells Au@$SiO_2$--CuS |
| 7 | 13 nm shells Au@$SiO_2$--CuS |
| 8 | 4 nm shells Au@$SiO_2$ |
| 9 | 17 nm shells Au@$SiO_2$ |
| 10 | 13 nm shells Au@$SiO_2$ |
| 11 | FTO-glass blank |

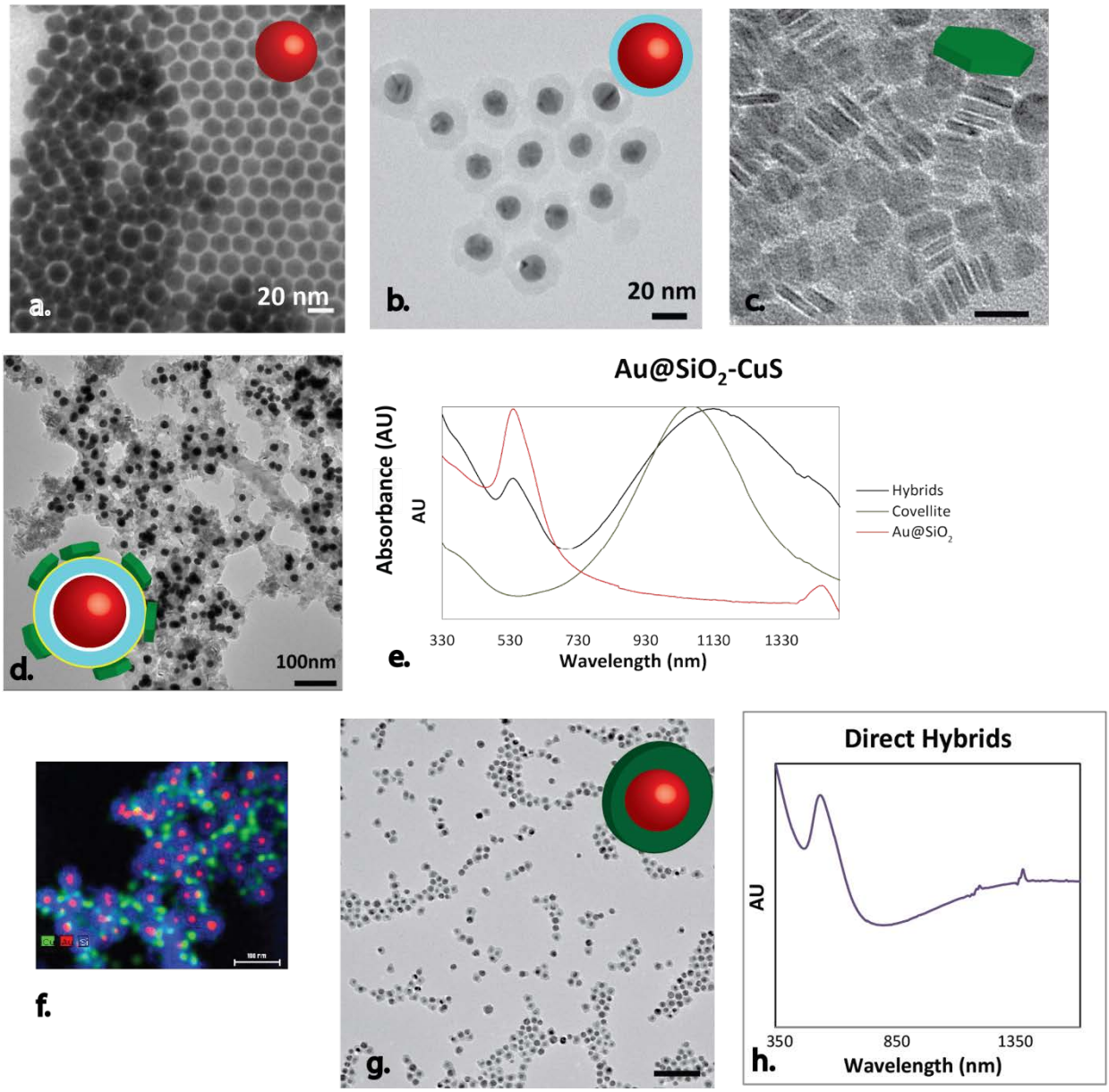


**Figure 7** a) Unshelled 16 nm Au NPs. b) Au@$SiO_2$ NPs. c) Covellite CuS NPs. d)Au@$SiO_2$--CuS e) sample of the UV-Vis spectrum of hybrid Au@$SiO_2$-CuS hybrids compared to CuS and Au@$SiO_2$. f) STEM-EDS elemental map of a Au@$SiO_2$-CuS hybrid superstructure. g) TEM of the direct Au-CuS hybrids h) UV-Vis of the direct hybrids showing NIR and visible LSPR peaks.

SHG measurements were carried out in collaboration with Roderick Davidson of the labof Professor Richard Haglund, physics dept. Additional details of SHG measurements, including analytical setup, are in Appendix B. Relative SHG potential is determined by measuring SH light at a series of different power intensities. The exponential fit of the curve generated at these different powers will be normalized to the sample's absorbance to give the

relative SHG efficiencies of the different hybrids. SHG was observed in most samples, with the exception of the first control, bare Au NPs. Hybrids sample raw data showed significantly more SHG than either plain Au@$SiO_2$ controls or the CuS controls, though further processing of the data is ongoing to generate quantitative results. An example of these results is included in Appendix B. While some samples began to lose second-order dependence at high laser intensities as higher-order effects predominated, many of the samples showed signs of thermal degradation at these same high (50 mW) excitation intensities. This burning of samples at high light intensity is fairly normal when the optical absorption is high, as it is for the CuS LSPR, especially since much of the plasmonic decay is thermal.[62,63] At the current time, these results still need to be normalized to account for differing particle density and loading, and varying film translucency. Also, though it is likely that the individual particles will not be discernable, Scanning Electron Microscopy (SEM) will be used to evaluate film thickness and uniformity and also to determine the extent of damage caused by the high-intensity laser to the films. Preliminary optical absorption measurements taken of the films have highlighted the necessity of quantifying scattering or reflectance of the films to enable meaningful interpretation of the relative strength of second harmonic generation by these samples.

## Conclusions

The hybrid Au@$SiO_2$-CuS synthesis reported upon here is a new synthetic route to form these hybrid systems. As compared to previously reported syntheses[27,49,50] for these types of Au@$SiO_2$-semiconductor hybrids, this synthesis has demonstrated higher quality (fewer multi-core particles, very limited agglomeration of core-shells) products at much thinner shell thicknesses than previously reported. The access to <10 nm shell thicknesses is a valuable addition to the existing literature, as the nature of plasmonic interactions changes quickly at this

distance scale.[64] The applicability of this synthesis to the widely-used citrate-capped Au NPs instead of CTAB-based Au syntheses also makes it valuable, as these syntheses produce high yields of clean, monodisperse particles. Furthermore, as demonstrated in the Au@$SiO_2$-$Cu_{2-x}Se$ examples presented herein, the dielectric barrier of the silica shell allows the creation of hybrid structures with two LSPRs preserved that unavoidably quench when hybridized through direct growth strategies.[44] Finally, the easy control over relative quantities of the respective nanoparticle precursors in the final product provides another variable to examine when studying NP-NP interactions.

This system is applied in this work to a study of plasmonic enhancement of SHG, but could easily be extended to the study of many different plasmon-NP interactions. The observation of SHG in the hybrid particles demonstrates the applicability of the system to LSPR-LSPR interactions.

# CHAPTER III

## PREPARATION OF GOLD SULFIDE NANOPARICLES *VIA* CATION EXCHANGE

Semiconductor nanocrystals (NC) have found wide applications due to their tunable band gap and high absorption coefficients. Semiconductor heterostructures allow even further tunability of material properties. Many current semiconductor NC applications, such as solar cells and photodiode arrays, rely extensively on the highly tunable cadmium and lead chalcogenides, and as a result the colloidal synthesis of these materials has been very well-developed.[65] However, these materials are highly toxic, and therefore the copper sulfides have been the focus of increased interest for semiconductor applications.[19,38,66–68] Copper sulfides display much promise for similar applications as lead and cadmium sulfides as they have a high absorption cross section with a direct band gap of 1.2-2.0 eV, ideal for biomedical and photovoltaic applications.[66,68] Furthermore, as their stoichiometry is tuned from $Cu_2S$ to CuS, copper sulfide nanoparticles exhibit strong localized surface plasmon resonance in the near IR, opening up further applications in optics, catalysis, and theranostics. These traits in addition to the low toxicity of copper sulfide have made it an appealing subject for study. Moving down the group eleven elements, $Ag_2S$ is also a direct band gap semiconductor that is widely used in nano- and macroscopic form for a wide range of applications.[69]

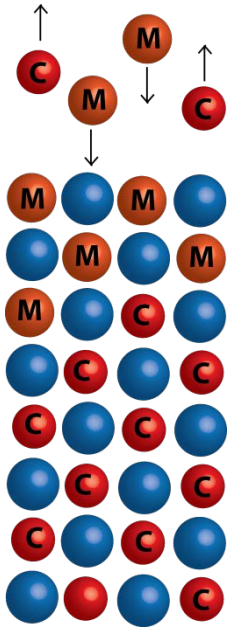


**Figure 8** Cation exchange, where original cation 'C' is replaced by new cation 'M.'

The group 11 sulfides CuS, $Cu_2S$ and $Ag_2S$ hold great promise for applications that take advantage of their direct band gaps in the visible region, high ion mobility, and surface plasmon resonance in the NIR when cation deficient. Another group 11 sulfide, gold sulfide, $Au_2S$, is has untapped potential. The crystal structure is cuprite, similar to α-$Ag_2S$ with a

body centered cubic anion sublattice. It is a *p*-type direct band gap semiconductor widely considered to be a promising candidate for many of the same applications as the other group eleven sulfides and in some cases surpass them.[70–72] Unlike $Cu_2S$ and $Ag_2S$, $Au_2S$ is not believed to be an ion conductor. Therefore it can be used in applications where leaching of ions is challenging, especially in thin films.[73] $Au_2S$ often forms at the interfaces between metal sulfides and Au, and so is an important material to understand for charge transport in thin film and hybrid nanomaterials.[74] While CuS, $Cu_2S$ and $Ag_2S$ are well studied, $Au_2S$ remains much more enigmatic.

On both the bulk- and nano-scale $Au_2S$ is a synthetically challenging material due to its metastability. Gold will readily reduce to metal rather than remain in the +1 oxidation state.[75] As a result, there are few direct colloidal syntheses of $Au_2S$,[72,76] and most result in a significant amount of metallic gold byproduct, hindering the material characterization. There is also poor control over product morphology which further leads to the instability.[70,71,75,77–81] Without reliable syntheses to clean, stable products, some of the fundamental material properties of $Au_2S$ are still a mystery. As an example, the band gap it is predicted to be within the wide range of 1.3-2.6 eV, and the basis of this prediction is not published.[82]

Reported syntheses of gold sulfide and gold-gold sulfide core-shell nanoparticles[78,83–85] are aqueous reduction of sodium sulfide and sodium gold sulphite,[70,72] reduction of chloroauric acid with sulphide ions[79,80], templated growth with apoferritin protein cages[76], and *via* controlled cation exchange[86]. The synthesis for $Cu_{2-x}S$—$Au_2S$ hybrids reported here falls into the latter category.

Nanoscale techniques give exquisite control over crystallite morphology, and by the nature of the colloidal syntheses, the most stable facets are exposed in high proportion and stabilized by

ligands. As a result, metastable phases and shapes can be kinetically trapped. Cation exchange, in particular, has frequently been applied to provide synthetic routes to otherwise unachievable product morphologies, such as in the synthesis of CuInS nanorods.[87] Cation exchange is practical for the alteration of nanomaterials, as this process occurs much more quickly on the nanoscale than at the bulk.[88–94] Cation exchange has recently been reported to yield $Au_2S$ and mixed gold sulfide hybrid nanocrystals from CdS and CuS nanoparticles.[86,95] $Cu_2S$ is an ideal template material for cation exchange as the crystal structure consists of a rigid anion sublattice with highly mobile $Cu^+$ cations.[19] Futhermore, there are synthetic techniques available to prepare large single crystalline copper sulfide nanocrystals with well-defined morphologies.[96] Here, we use nanoscale cation exchange to achieve $Au_2S$.

A cation exchange procedure was used to transform $Cu_2S$ chalcocite nanoplatelets to hybrid $Cu_2S$-$Au_2S$ "nanostars" and to single- and hexa-crystalline $Au_2S$ nanocrystals. This templated design allows control over the final product size, composition, and shape. The work reported herein provides an easily controllable synthetic route to $Au_2S$ nanocrystals as well as new understanding of the kinetic and thermodynamic variables at work in this exchange. The nature of cation exchange produces an $Au_2S$ product with crystallinity and purity not matched by any synthesis currently published. The enhanced stability of the large disk-like crystals reported facilitates material characterization not previously possible. Remarkably, this is the first report of the absorbance spectra of $Au_2S$ alone, and through a Tauc plot, the first reported experimental bandgap.[72,86]

$Cu_2S$ platelets were synthesized via a modified literature method (Figure 9) .[97] A copper thiolate precursor solution [(copper (II) nitrate(0.9mmol), tetraoctylammonium bromide (TOAB)(0.3 mmol), and dodecanethiol (DDT) (1.0 mmol)] was heated in an oil bath under

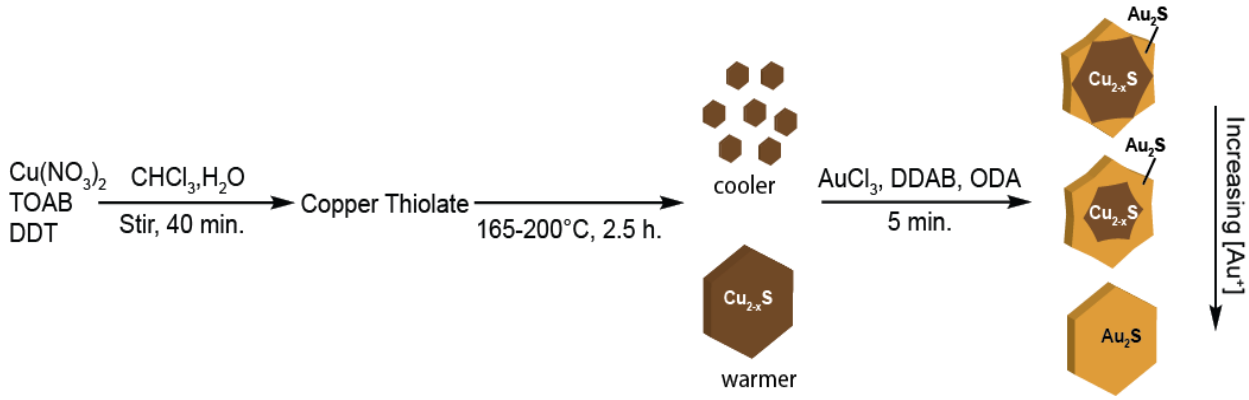


**Figure 9** Synthetic scheme for $Au_2S$

atmosphere for 30 min – 2.5 hours. At the low synthetic temperatures of 165°C, highly monodisperse hexagonally shaped $Cu_2S$ platelets with basal short axis of ~10 nm were prepared. At higher synthetic temperatures of to 200°C, larger hexagonal plates with basal short axis of 50-200 nm were prepared and with a much greater size distribution. XRD indicates the phase is low chalcocite $Cu_2S$. Low chalcocite has a large unit cell with low symmetry, but for convenience of discussion can be approximated as the closely related high chalcocite phase, which has a hexagonal unit cell.[98] HR-TEM indicates that the large faces of the particles are the (001) plane of the hexagonal $Cu_2S$, which has hexagonally arranged S atoms.

Cation exchange was performed through the slow addition of a solution of gold (III) chloride (0.03 mmol), didodecyldimethylammonium bromide (DDAB), and toluene to a solution of $Cu_2S$ nanocrystals in oleylamine (OlAm) and toluene under nitrogen atmosphere. (Details in Appendix C). The gold precursor solution changed color from dark orange to colorless upon contact with nanoparticle/OlAm solution (Appendix C) The complete quench of the characteristic $Au^{3+}$ absorption indicates the OlAm acts to quickly reduce the $Au^{3+}$ to $Au^{1+}$, readying it for exchange with the $Cu^{1+}$ of the copper sulfide.

The product of the exchange is disks of $Au_2S$ with the same morphology as the parent $Cu_2S$. The XRD shows the expected $Au_2S$ phase, consistent with that reported by Ishikawa et al and other.[73,86] FFT analysis of lattice fringes from HR-TEM identified several d-spacings corresponding to $Au_2S$, specifically 0.36 nm (110) and 0.29 nm (111). (Figure 10) The top face of the $Au_2S$ crystals therefore belong to a related (110) plane, which is a direction with hexagonally arranged sulfur atoms in the BCC anion lattice of the cuprite crystal structure of $Au_2S$.

Exchange from small $Cu_2S$ (10-20 nm diameter) nanocrystals yield single-crystalline $Au_2S$. When less Au precursor was added small disks 10-30 nm appear as two sided Janus $Cu_2S/Au_2S$ particles. Together, this suggests that small particles undergo a unidirectional exchange process originating from one side of the $Cu_2S$.[91] In contrast, exchange into larger $Cu_2S$ nanocrystals (>20nm) results in a hexa-crystalline product indicating six separate directions of exchange. With less Au precursor added, the result was hexagonally shaped $Cu_2S$ disks "tipped" with $Au_2S$. Larger particles, therefore, are thought to go through exchange through six independent directions.

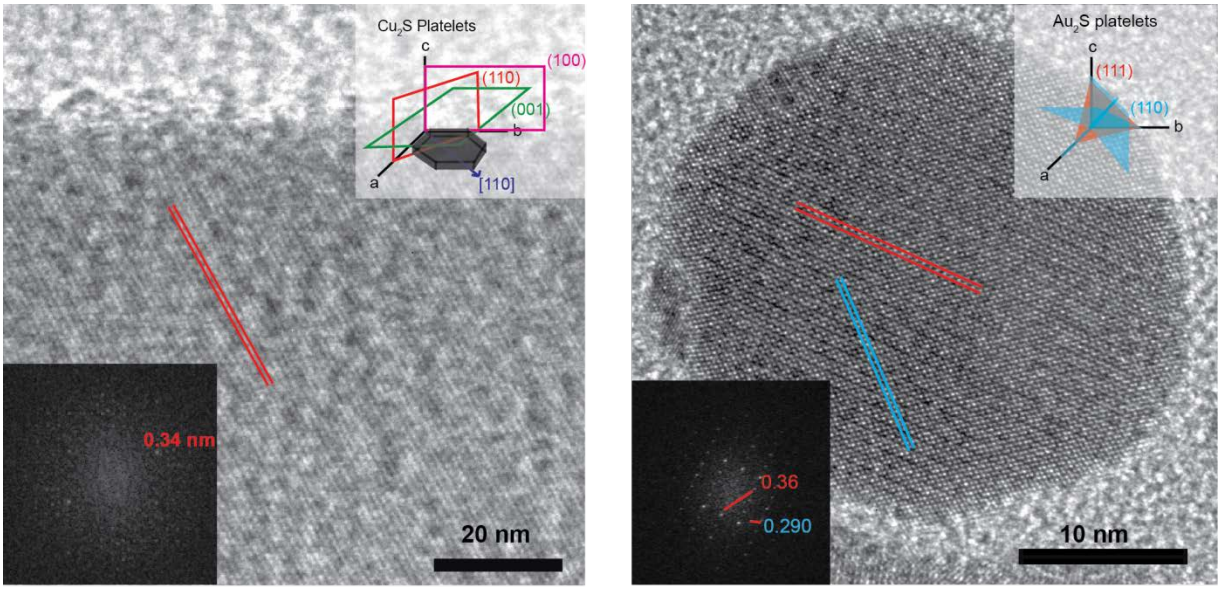


**Figure 10** a) HR-TEM of top face of $Cu_2S$ platelet. b) HR-TEM of completely exchanged $Au_2S$ platelet

Bright field TEM of the larger particles after exposure to low Au precursor concentrations shows that the exchange occurs exclusively from the tips of the hexagonal copper sulfide platelets. The direction of growth corresponds to the <110> directions of the $Cu_2S$, resulting in triangular tips of gold sulfide surrounding copper sulfide centers. As the size of cationic $Au^{1+}$ (r = 137pm) is much larger than $Cu^{+}$ (r = 77pm),[99] visible strain deforms the hexagonal platelets into pointed star shapes as the $Au^{+}$ exchanges for $Cu^{+}$. Further evidence of the directional nature of this exchange is seen in figure 11f in the presence of lines of $Au_2S$ across the surface of the copper sulfide cores, presumably corresponding to surface step defects of the $Cu_2S$.

The highly directional nature of the cation exchange is related to the shifts in the anion lattice upon exchange. The transition from the HCP to BCC anion sublattices of the hexagonal chalcocite and cuprate crystal structures, respectively, requires an expansion in the <110> directions of the $Cu_2S$ lattice.[100] These directions correspond to the tips of the parent Cu2S nanocrystals facilitating the exchange along these axes.

There are pronounced domain boundaries at the 'seams' where two corners of $Au_2S$ meet. The TEM of many large particles show at least one low contrast "seam" where two corners meet or a "crack" at an edge in the fully exchanged $Au_2S$. These are likely ion channels for $Cu^{1+}$ to escape the structure during the exchange process, directionally along the [100] of the $Cu_2S$.[101] It is interesting to note that neither the $Au^{3+}$ inclusion, nor $Cu^{1+}$ leaching occur through the (001) faces of the $Cu_2S$ indicating there is poor ionic conductivity in this crystallographic direction.

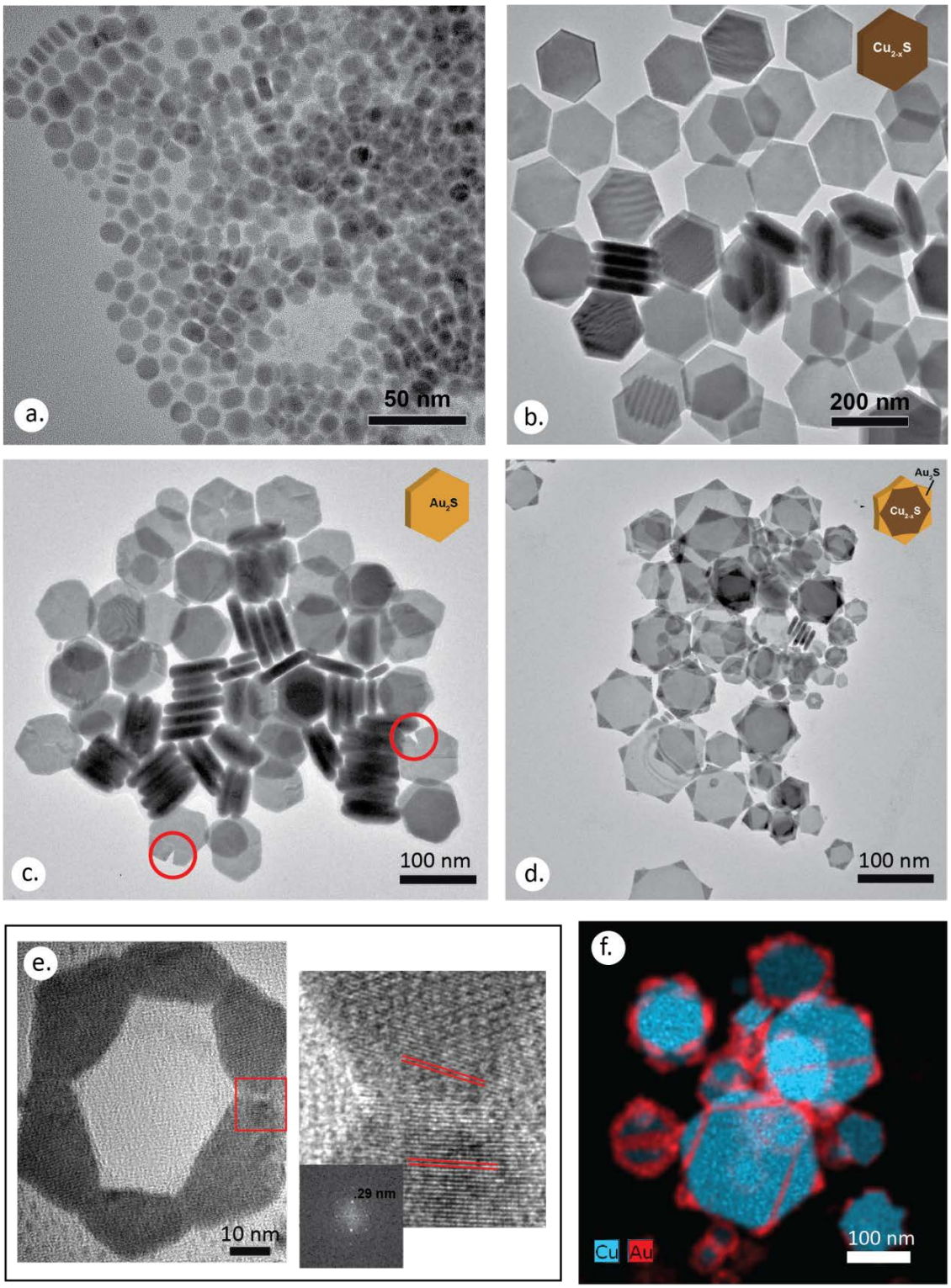


**Figure 11** TEM images showing: **a.** Smallest size $Cu_2S$ platelets, planar width of 11±2 nm. **b.** Large $Cu_2S$ platelets, planar width of 200 nm. **c.** Almost completely exchanged $Au_2S$ platelets. Red circles highlight cracks along domain boundaries due to strain following exchange. **d**. P artially exchanged $Au_2S$—$Cu_{2-x}S$. **e**. $Au_2S$ ring remaining post-etching with neocuproine. The red lines highlight the (110) lattice fringing on two adjacent crystallites, clearly showing the misalignment at these interfaces. **f.** STEM-EDS map clearly showing cation exchange confined to the (110) faces of the $Cu_{2-x}S$ and step defects on the surface of the platelets exposing the (110) face.

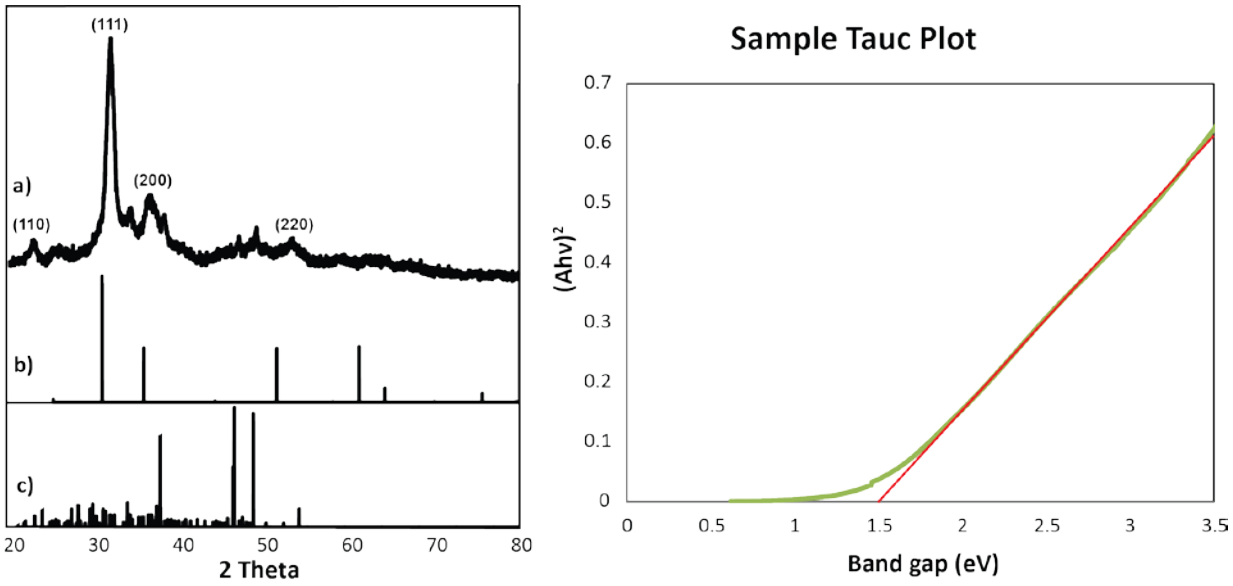


**Figure 12** (Left) Powder XRD of a) $Au_2S$—$Cu_2S$ hybrid sample with b) $Au_2S$ card and c) djurleite card for reference. (Right) Two examples of Tauc plots derived from absorption spectra of pure $Au_2S$ nanoparticle samples.

Further morphologies such as triangles and rings of $Au_2S$ were attained by limiting the extent of exchange to yield $Cu_2S$- $Au_2S$ hybrids and followed by the removal of $Cu_2S$ domains by etching the $Cu^+$ with an excess of neocuproine (Figure 11e) The removal of any remaining $Cu_2S$ was confirmed through TEM, EDS and XRD. The extreme flexibility in template size and control over the extent of cation exchange makes the synthesis reported here the first procedure that offers a wide range of possible product morphologies.

A noteworthy missing piece in our knowledge of gold sulfide is an established experimental band gap. A Tauc plot analysis of UV-Visible absorption data was used to measure the band gap as seen in figure 12. $Au_2S$ nanoparticles were stirred with neocuproine in an acetone/ toluene solvent system in order to remove any trace copper before UV-Vis data was collected. As $Au_2S$ is a direct band gap material, $(\alpha hv)^2$ as estimated by $(Ahv)^2$ was plotted versus the energy in eV. The x-intercept of the linear region of these plots was established to consistently fall at about 1.5 eV. This result was repeated in excess of 5 times.

The balance of cation exchange vs. metal reduction is well established to be highly system-specific for metals with high electron affinity like Au. There are many factors at play in addition to relative free energies of formation such as relative solubilities, ligand chemistry, nanocrystal size and shape, and lattice strain.[88] A simple thermodynamic calculation (Appendix C) shows that the Gibbs Free Energy change for cation exchange in this case is favorable[95] and experimentally the cation exchange is completed within five minutes. While reduction of $Au^{1+}$ to $Au^0$ is also thermodynamically favorable, it is much slower than the cation exchange process; stirring the precursor solution with an excess of OlAm in the absence of template particles quickly converts the $Au^{3+}$ to $Au^{1+}$, but metal nanoparticle formation only occurs after several days of stirring at room temperature. (See Appendix C)

$Au_2S$ is prone to decomposition to Au(0) under X-ray and electron beam exposure. For instance, XPS characterization of the product (Appendix C) shows the presence of only Au (0) due to the intense extended exposure to X-rays inherent to the technique (Al $K_a$, 1486 eV). It has also been noted that the surface Au tends to more easily reduce, in this work and others,[80] and this may also be the case here as XPS is a surface sensitive technique (inelastic mean free path of a 1480 eV electron in Au is about 1.8 nm)[102]. However, we do note that an increase in size of the crystallites of $Au_2S$ stabilizes the material towards under X-ray and electron beam flux. With extended exposure to the electron beam of the TEM (on the order of 3 min for the small, 10 nm $Au_2S$ NC and ~10 minutes for the larger >50 nm disks), high-contrast islands of Au (0) formed, which is consistent with previously reported syntheses of $Au_2S$. XRD analysis (Cu $K_a$, 8027 eV, 1.8 kW, 8 h) of samples after reaction show only $Au_2S$ peaks for the large crystallites, with small peaks corresponding to unexchanged copper sulfide. For small crystallites, there is contamination from Au(0) due to decomposition. (Figure 12)

Therefore, the stability of the product can be tuned by changing the size of the product, with large (> 100nm) platelets remaining stable under TEM and XRD, and smaller platelets with their greater surface-area-to-volume ratio and concomitant higher degree of disorder tending to reduce rapidly. The previous reports of cation exchange[86,95] to produce $Au_2S$ lacked any kind of directional control, so the products were therefore invariably polycrystalline and were reported to rapidly reduce in TEM.

A major barrier to the study of $Au_2S$ nanoparticles has been the lack of a synthetic route to a high-quality, single crystalline product without the presence of side products such as metallic gold. We have presented a highly versatile synthesis for $Au_2S$ and $Au_2S$-$Cu_2S$ hybrid nanoparticles, adaptable to a wide range of product morphologies and compositions. We have also presented the first (known to us) experimental band gap value for $Au_2S$. This synthesis paves the way for further study of $Au_2S$ in the field of semiconductor nanoparticles.

## Appendix A: Synthetic Detail for Chapter I

### General

All glassware for use in non-aqueous syntheses was oven dried before use and air-free reactions were carried out on a Schlenk line under nitrogen. A J-Kem Model 210 temperature controller was used in conjunction with heating mantles for most semiconductor reactions. Other heating methods are noted as used.

UV-Vis data for all nanoparticles was collected on a Jasco V-670 UV-Vis spectrophotometer with a baseline run of atmospheric conditions prior to data collection. 1 cm glass cuvettes were used with the exception of studies requiring fluorescence data, in which case1 cm quartz cuvettes were used. Fluorescence data was collected on a Jasco FP-8300 fluorimeter.

TEM grids were prepared by dropping 10 μL of NP solution onto a grid resting on filter paper, except where otherwise noted. TEM images were collected on a CM20 or Osiris instrument at 200 kV.

All solvents and reagents were used as received. Copper sulfide nanoplatelets and Jiang hybrids were stored for later use by freezing in cyclohexane.

A Time Bandwidth Products 1053 nm laser with a bandwidth of 6nm FWHM and a pulse width of 100 fs was used in SHG measurements. Signal detection was carried out with a Hamamatsu photomultiplier tube (PMT) connected to a Stanford Research Systems photon counter. Power was controlled with crossed Thorlabs linear polarizers.

**Initial synthesis.** $Cu_2Se$ NP stock solution was prepared using a published synthesis.[62] In short, CuCl (0.1976g, 2mmol), 5mL octadecene, and 5 mL oleylamine (OlAm) were degassed at 60˚C for at least one hour. In a nitrogen environment, selenourea (0.1463 g, 1mmol) and 1.2 mL OlAm were placed in a 10 mL round-bottomed flask, then the flask was transferred to a Schlenk line and purged three times with $N_2$. The copper chloride solution was heated to 130˚C and the selenourea solution to 200˚C. Each solution was held at their respective temperature for 10 minutes, then cooled to 100˚C and 160˚C, respectively. The selenourea solution was then injected into the copper solution and the reaction temperature was increased to 240˚C and held for 30 minutes. The reaction was cooled to room temperature, then the product was cleaned via precipitation of product with isopropyl alcohol (IPA), collection through centrifugation, and resuspension in toluene. All solvent additions and opening of the vial occurred in a glovebox. This synthesis yielded 10.7 ± 2.2 nm particles (n = 300).

**Second synthesis.** A more reliable $Cu_{2-x}Se$ synthesis for creating more monodisperse, predictable particles was found in the literature.[18] In short, trioctylphosphine-copper (TOPCu) and trioctylphsophine-selenium (TOPSe) precursors were simultaneously injected into a 300˚C mixture of trioctylphosphine oxide (TOPO) and octylphosphonic acid (OPA). The temperature is decreased to 285˚C and held for 13 min, and then the reaction was quenched via injection of degassed toluene. The product was centrifuged in toluene for 20 minutes to remove any bulk

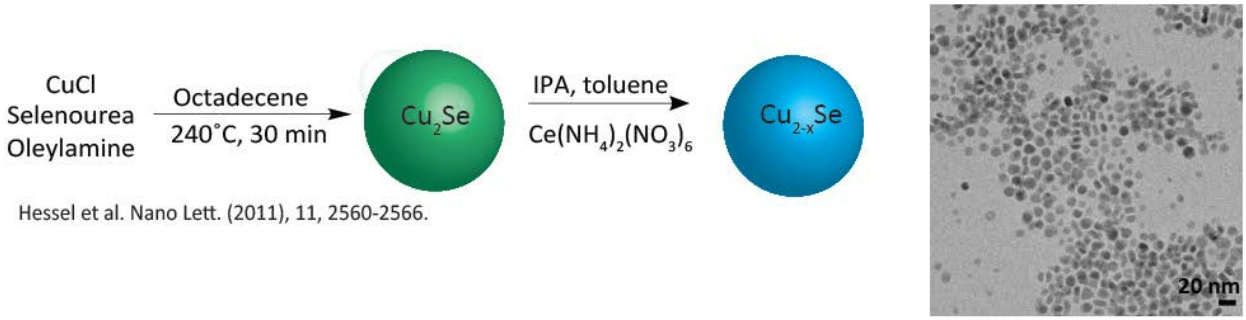


**Figure 13** Reaction Scheme for copper selenide nanoparticles and TEM

product, then 2 mL acetonitrile was added to the supernatant and it was centrifuged for another 20 min. Finally, methanol (MeOH) was used to precipitate the remaining nanoparticles from the supernatant, and they were redispersed in toluene, washed one more time with MeOH, and finally stored in toluene. The particles produced in this synthesis were far more regularly-shaped and monodisperse (d = 9.3 ± 1.2 nm, n = 129) than those from the earlier Au—$Cu_{2-x}Se$ synthesis, and will be used in the Au@$SiO_2$—$Cu_{2-x}Se$ synthesis.

## Copper sulfide syntheses

**Covellite copper sulfide**. Covellite copper sulfide (CuS) nanoparticles were synthesized via a literature procedure[37]. CuCl (49.5 mg, 0.5 mmol), Octadecylamine (ODE, 7.68 mL), oleylamine (OlAm, 1.97 mL), and oleic acid (OLAC, 0.21 mL) were added to a 25 mL three-neck round-bottom (RB) flask, and rapidly heated to 130 ˚C, where they were held for ten minutes under vacuum. The flask was then filled with $N_2$ and heated to 180˚C. 2mL of a stock 1 M sulfur-oleylamine (S-OlAm) solution was injected, the temperature was recovered to 180˚C and held for 10 minutes before cooling the flask by spraying the outside with toluene. A modification to this synthesis that improved final product quality was to heat the ODE, OlAm, and OLAC to 100˚C in the 25 mL RB flask and holding under vacuum for thirty minutes to remove dissolved gases and water, then flushing the flask with nitrogen and adding the CuCl. After this point, the synthesis was continued as published.

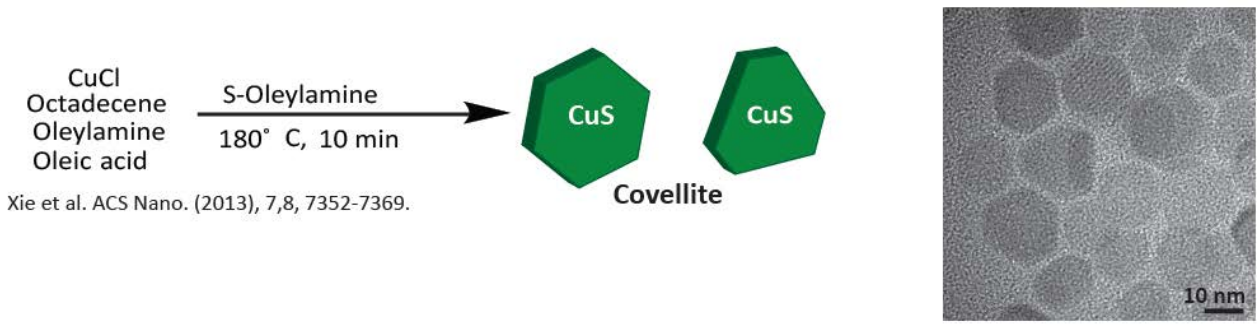


**Figure 14** Reaction scheme for covellite copper sulfide and TEM

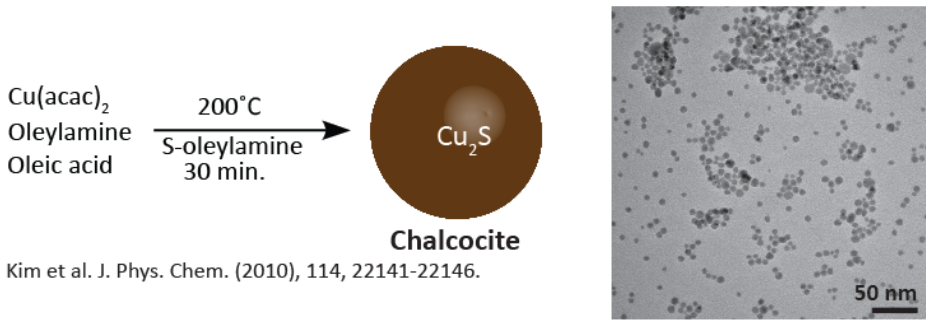


**Figure 15** Reaction schemes for chalcocite platelets and spheres and TEM.

**Copper sulfide spheres**. Copper sulfide spheres were synthesized per a modified literature synthesis[103] as a control for the direct hybrid synthesis. Copper (II) acetonacetate ($Cu(acac)_2$, 0.27 g, 1.0 mmol), OlAm (10 mL), and OLAC (5 mL) were put in a 25 mL 3-neck RB flask and held with stirring under vacuum for one hour at room temperature to remove dissolved gasses. The mixture was heated to 200˚C under $N_2$ and an S-OlAm solution (16 mg S, 1mL OlAm) was injected, then the temperature was held at 200˚C for 30 minutes. Dark brown product particles were washed with MeOH and toluene.

## Hybrid syntheses

**Gold addition**. In order to grow Au domains[45] on the $Cu_2Se$, $2.35 \cdot 10^{-7}$ mmol $Cu_2Se$ ($\epsilon = 1.59 * 10^7$), 19 mL toluene, and 1 mL OlAm were added to a 50 mL round-bottom flask in a glovebox. Also in the glovebox, $AuCl_3$ (8.2 mg, 0.03 mmol) and 4 mL toluene were added to a 10 mL RB flask already containing 35.6 mg dodecylamine (DDA) and 62.4 mg didodecyldimethylammonium bromide (DDAB). Both flasks were removed from the glovebox. The $Cu_2Se$ NP solution was transferred to a Schlenk line, and the $AuCl_3$ solution was sonicated for 10 minutes to ensure complete dissolution of all components. The $AuCl_3$ solution was added dropwise to the $Cu_2Se$ solution over 3 minutes with vigorous stirring. Product particles were precipitated with methanol and resuspended in 200:1:1 toluene:OLAM:TOP solution. In order to

synthesize oxidized $Cu_{2-x}Se$ NPs for hybrid synthesis, $Cu_2Se$ particles were chemically oxidized with ceric ammonium nitrate. Temperature varied syntheses were carried out in ice water or dry ice/acetone baths instead of at room temperature.

Later experiments showed little to no signs of air sensitivity, so fewer precautions were taken to avoid the exposure of the particles to air, particularly in the case of particles that were stored in air for several days with no adverse effects or change in optical properties, such as all of the copper sulfide examples. The Au/DDA/DDAB solution was prepared in an air-free manner, and the particles were added to the reaction flask with the OlAm, which was then placed under vacuum at room temperature to remove excessive dissolved gases and flushed with nitrogen. For copper sulfide samples, nanoparticle concentration was recorded by taking a UV-Vis of the toluene/NP/OlAm solution before adding the Au growth solution, but no evidence of a NP concentration dependence was observed.

**Gold-seeded direct hybrids**[43] **and controls**. Au seed particles were synthesized by injecting $HAuCl_4$ (0.3 mmol, 124 mg) in 1 mL OLAM (70%) into 5 mL OlAm previously held at 150 ˚C under nitrogen for 20 min. After Au injection, the reaction was stirred at 150˚C for 90 min, then cooled to room temperature naturally. Product particles were cleaned via precipitation with EtOH followed by centrifugation and resuspension in hexanes.

Copper stearate was prepared by dissolving $CuCl_2$(1.1g) and sodium stearate (4.75g) in methanol separately, then adding the two solutions together and heating to 70˚C for 3 hours. The dark green CuCl solution instantly turned vivid blue and a cloudy precipitate appeared upon mixing with the clear sodium stearate solution. Product was collected by adding water to the methanol solution, then washing several times with MeOH and $H_2O$ and drying under vacuum to obtain a light blue powder.

Hybrids were synthesized by adding 0.2 mmol seed Au NPs, Cu-Stearate (62.7 mg), and trioctylamine (5 mL) to a 25-mL three-neck RB flask and stirring for 30 minutes under $N_2$. The reaction mixture was then heated to 80˚C, and 0.75 mL of a solution containg S powder (8 mg), 1,2-dichlorobenzene (0.5 mL), and OlAm (2 mL) was added dropwise very slowly. The reaction flask was then heated to 100˚C for 1 hour, cooled naturally, and the purple-black particles were purified with hexanes and ethanol (EtOH).

The copper sulfide control to these hybrids was prepared by adding Cu-stearate (188 mg) to trioctylamine (5 mL) and stirring 30 minutes under $N_2$. The solution was then heated to 80˚C under a clear dark green solution formed. 0.75 mL of a solution containg S powder (12 mg), 1,2-dichlorobenzene (0.25 mL), and OlAm (1 mL) was added dropwise very slowly. The reaction temperature was raised to 100˚C and held for 1 hour before being allowed to cool to room temperature. Particles were cleaned with hexanes/EtOH and centrifugation. The product was a greenish black color.

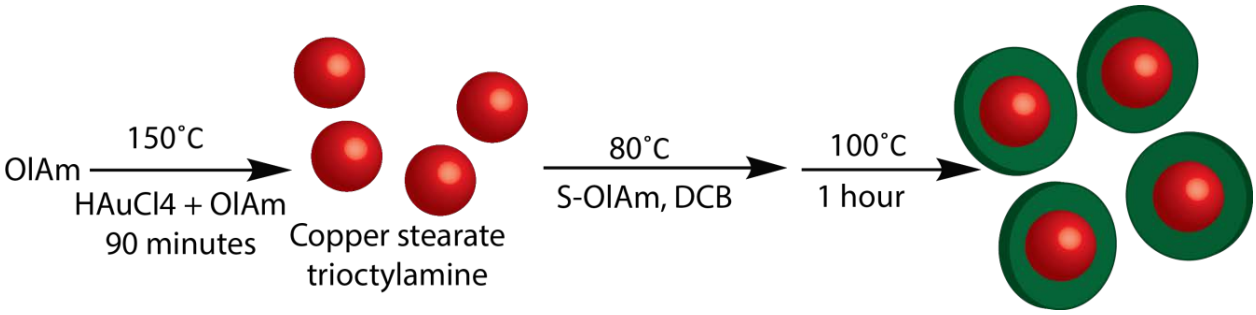


**Figure 16** Direct hybrid synthesis for control

### Au@$SiO_2$ core-shell nanoparticles

Two syntheses were used to synthesize Au@$SiO_2$ core-shell nanoparticles. The first synthesis consisted of a seeded gold nanoparticle CTAB reduction and shells formed via base-catalyzed tetraethylorthosilicate (TEOS) polymerization. The second synthesis consists of a Turkevich-style citrate reduction of chloroauric acid followed by exchange of capping citrate

with (3-aminopropyl) trimethoxysilane (APTS) and shell growth via the addition of a sodium silicate solution activated via lowering the pH.

**Synthesis 1 details.** The first method employed in the synthesis of $Au@SiO_2$ core-shell nanoparticles was adopted from Khanal et al. (2012).[49] First, spherical Au NPs were prepared ranging in size from 5-40 nm following a literature synthesis.[57] 3.5 ± 0.7 nm (n = 103) gold seed nanoparticles were synthesized through the addition of 0.6 mL ice-cold $NaBH_4$ (0.1 M ) solution to an aqueous solution of $HAuCl_4$ (1.7 mg) and trisodium citrate (1.47 mg). The solution was stirred for 3 hours before use to ensure decomposition of the $NaBH_4$. $HAuCl_4$ (17.03 mg) was dissolved in 200 mL $H_2O$, and then cetyltrimethylammonium bromide (CTAB, 6 g) was added and the solution was heated until the CTAB was completely dissolved, yielding a bright orange solution to be used as a growth solution. To grow particles, seeds were added to a mixture of growth solution and ascorbic acid. Ascorbic acid is not a strong enough reducing agent to form Au particles without the presence of seeding particles.

| **Synthetic strategies for different particle sizes** | |
|---|---|
| **Particle Size** | Synthetic components |
| **5 nm** | 2.5 mL seed solution, 7.5 mL growth solution, 0.05 mL 0.1 M ascorbic acid |
| **7 nm** | 1.0 mL seed solution, 9 mL growth solution, 0.05 mL 0.1 M ascorbic acid |
| **16 nm** | 1.0 mL 7 nm particles, 9 mL growth solution, 0.05 mL 0.1 M ascorbic acid |
| **35 nm** | 1.0 mL 16 nm particles, 9 mL growth solution, 0.05 mL 0.1 M ascorbic acid |

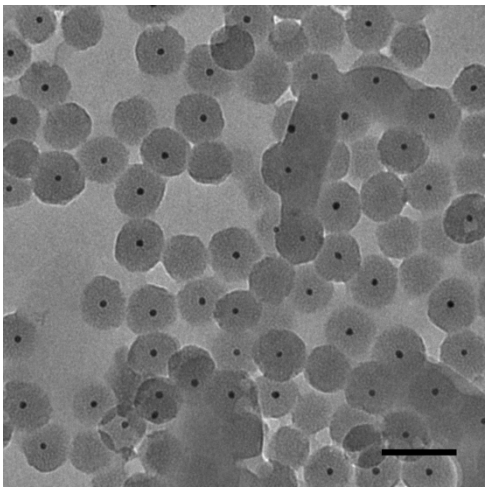

**Figure 17** The most successful synthesis of $Au@SiO_2$ NPs following the procedures used by Khanal et al. Note thick (30+nm) shells and numerous $SiO_2$ particles without cores (scale=100nm)

Particles were cleaned via high-speed centrifugation and resuspension in DI $H_2O$. The smaller particles were mostly spherical; however, at the largest particle size rods and tetrahedral particles began to form a significant fraction. $SiO_2$ shells were grown on these particles following a sol-gel method.[49] To 30 mL nanoparticle solution containing approximately $10^{-11}$ moles of nanoparticles, 50 μL of NaOH (0.1 M) was added. After 5 minutes, 50 μL 20% TEOS in methanol was added drop-wise with slow stirring. After 8-12 hours, the additions could be repeated in order to generate thicker shells. Unfortunately, this synthesis was difficult to reliably reproduce, and produced shells that were too thick, so a different synthesis was found.

**Synthesis 2 details** The most successful Au@$SiO_2$ core-shell particle synthesis[8] began with a Turkevich[56]-type reduction of chloroauric acid to form citrate-capped gold nanoparticles. Briefly, 425 mL of DI $H_2O$ was brought to a boil in a 1 liter Erlenmeyer flask. $HAuCl_4$ (43.2 mg) was dissolved in 50 mL $H_2O$ and added to the boiling water. After the solution returned to a boil, trisodium citrate(0.25g ) dissolved in 25 mL $H_2O$ was added with vigorous stirring and the solution was boiled for 30 more minutes, progressing from grey to purple to a dark red color as the nanoparticles nucleated and grew. This synthesis yielded citrate-capped gold nanospheres about 16 nm in diameter. To grow 2-4 nm $SiO_2$ shells on these particles, 2.5 mL of 1 mM APS in MeOH was added to 500 mL of unaltered gold nanoparticle solution in order to displace citrate capping ligands and form a surface upon which $SiO_2$ could condense. The solution was vigorously stirred for 15 minutes, then a solution of sodium silicate (adjusted to pH 10) was added, resulting in a final solution pH of 8. Stirring was reduced to a minimum speed and continued for 4 days to ensure shell formation. At this point, $SiO_2$ shells were present on the gold nanoparticles. In order to increase shell thickness, varying volumes of TEOS and 2 mL $NH_4OH$ were added, as well as 100 mL ethanol, and the solution was slowly stirred for a minimum of 2

days. Particle progress was monitored at each step with TEM and UV-Vis. This synthesis provides a facile method of creating shells of any desired thickness from 2 nm up.

## Silica shell functionalization

**Transfer of $Au@SiO_2$ particles to nonpolar organic solvent.** Transfer of $Au@SiO_2$ particles to chloroform was accomplished following a published procedure with some modifications.[8] An excess of 3-(trimethoxysilyl)propyl methacrylate approximately equivalent to the quantity of silica already present in the NP dispersion was added. This was stirred at room temperature for 45 minutes before slowly distilling off about 100 mL of the solvent over the course of one hour. At this point, a small aliquot would be withdrawn and tested for functionalization by adding $CHCl_3$ and visually accessing the transfer of the nanoparticles to the $CHCl_3$ layer. If the particles did not transfer from the $H_2O$/EtOH solvent mixture to the $CHCl_3$, refluxing would be continued until they did. This functionalization step did not significantly increase shell thickness (remained within standard deviation of original values). Once functionalized with methacrylate, the particle stability was much improved. The particles could be concentrated and collected via polar solvent addition and centrifuging, and could be stored in a mixture of EtOH and $CHCl_3$ for months without irreversibly agglomerating or experiencing any change in optical properties as the unfunctionalized particles had a tendency to do.

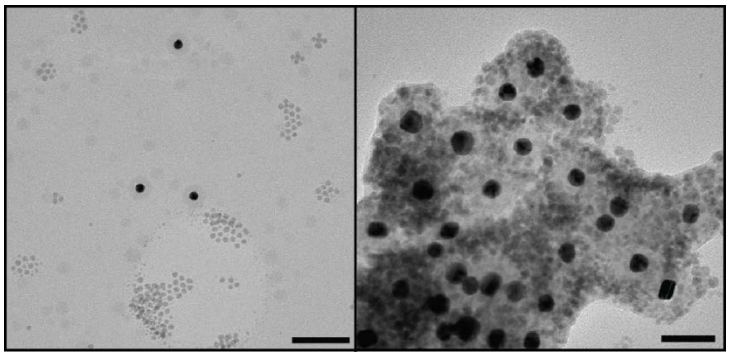

**Figure 18** left) methacrylate-functionalized $Au@SiO_2$ and $Cu_{2-x}Se$, showing no signs of attachment of $Cu_{2-x}Se$ (scale=100nm). right) amine and methacrylate functionalized $Au@SiO_2$ mixed with $Cu_{2-x}Se$, showing attachment of all $Cu_{2-x}Se$ to the $SiO_2$ shells. (scale=50nm)

**Amine functionalization of $Au@SiO_2$**[49,52,61] Amine functionalization of methacrylate-functionalized $Au@SiO_2$ was accomplished via adding 100 µL of APTES to a solution of $Au@SiO_2$ in EtOH, stirring at room temperature for 12 hours, and then refluxing. The particles were then collected via centrifugation and the extent of surface functionalization was accessed by adding CuS or $Cu_2Se$ to a solution of the $Au@SiO_2$ in THF and stirring for thirty minutes, then collecting the $AuSiO_2$ via centrifugation and examining the attachment of copper chalcogenide NPs to the $SiO_2$ surface via TEM. When the surface was appropriately functionalized, no free copper chalcogenide NPs would be visible and large superstructures consisting of $Au@SiO_2$/CuS agglomerations would dominate. These agglomerations only appeared with the addition of copper chalcogenide NPs and were due to CuS NPs adhering to the surface of multiple $Au@SiO_2$ particles.

## Hybrid superstructure preparation

To prepare hybrid superstructures, plasmon peak intensity of $Au@SiO_2$ and CuS solutions were measured via UV-Vis, then CuS was added to a solution of $Au@SiO_2$ such that the proportion of plasmon peak intensity Au:CuS (530 nm:1050 nm) was approximately 1:2.

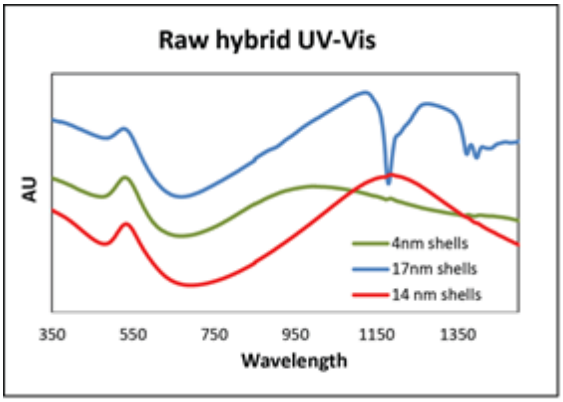


**Figure 19** UV-Vis spectra of hybrid superstructures in solution

## SHG sample preparation

Fluorine-doped tin oxide-coated glass slides were cut into 1.75 cm diameter circular disks. The disks were fit into the bottom of 6-dram glass centrifuge vials with the conductive FTO facing

upwards, and a suspension of each NP or hybrid sample in THF was added to the vials. The vials were then placed a 4400 rpm centrifuge, and spun until the samples had formed an even pellet onto the FTO surface. The solvent was then carefully pipetted out of the vial, and characterized by UV-Vis to determine if any NPs had remained in solution. The pellet was slowly dried out in the vial, then removed and placed into a vacuum dessicator over Drierite. Samples were stored under vacuum until SHG was evaluated, and then replaced under vacuum until all reflectance, transmission, scattering, and SEM evaluation was completed to minimize sample oxidation and degradation.

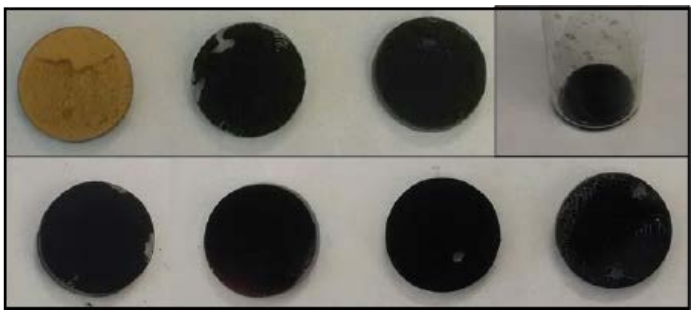

**Figure 20** Clockwise from top left: Gold and copper sulfide blanks and direct hybrids; a 6-dram vial containing a freshly prepared film, and all three core-shell hybrids and the covellite CuS sample.

# Appendix B

## SHG Analysis Apparatus

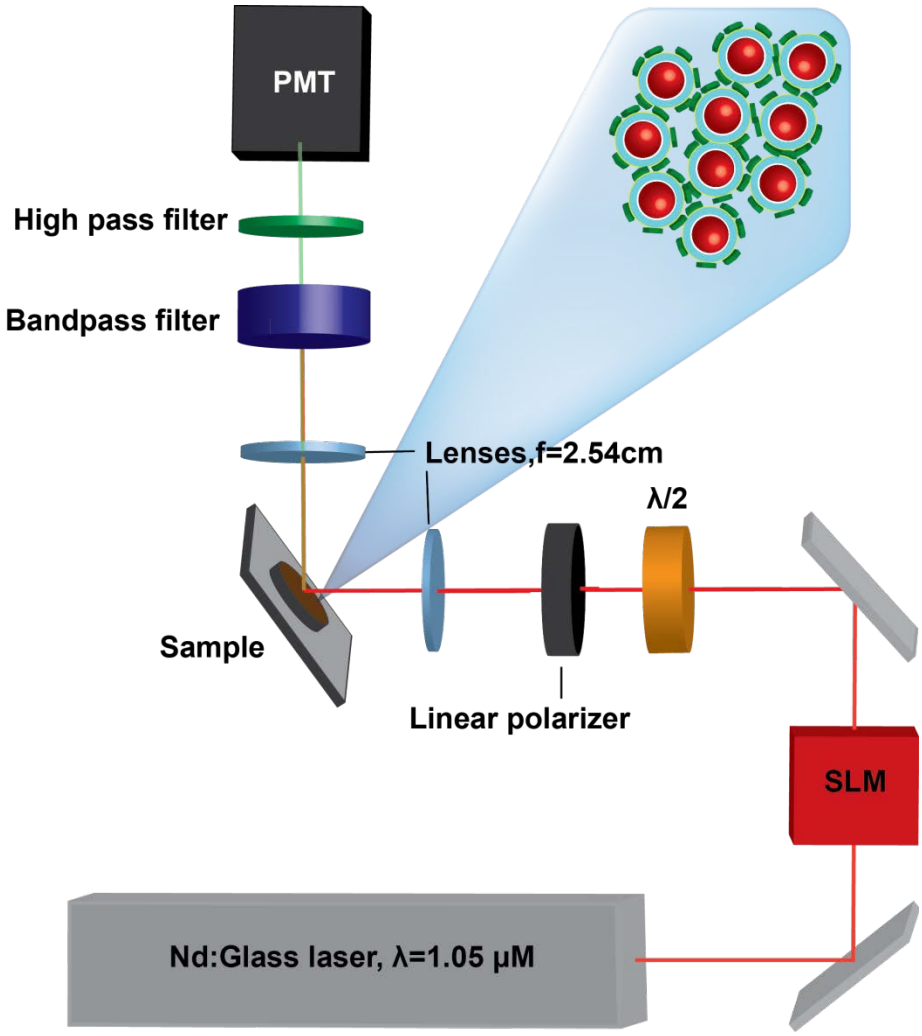


**Figure 21** Laser setup for SHG analysis. PMT = photomultiplier tube. SLM = Spatial light modulator

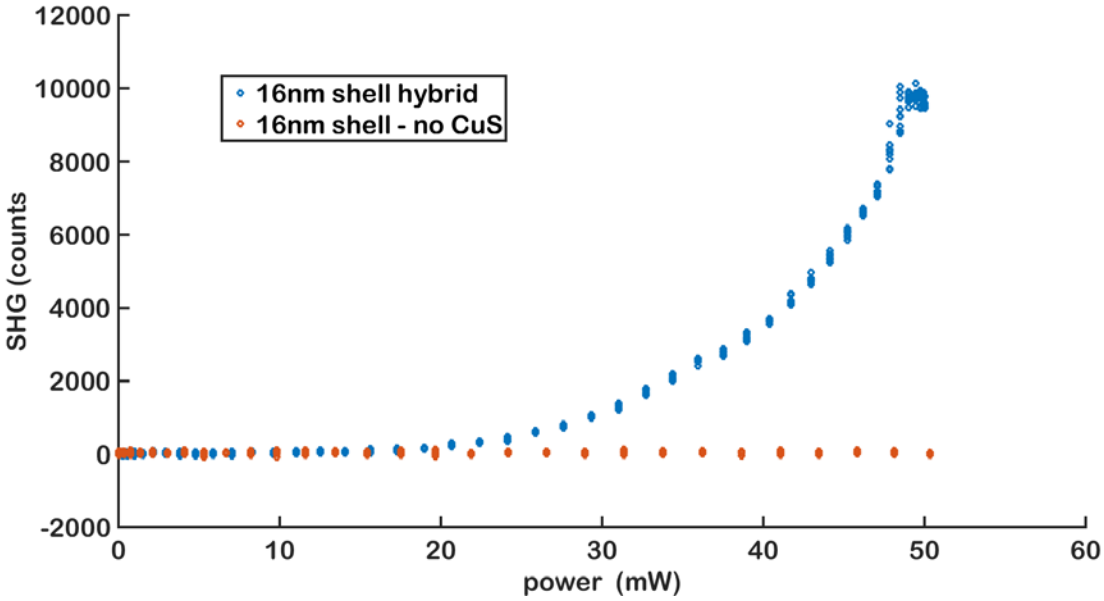


**Figure 22** An example of the SHG enhancement observed in the hybrid Au@$SiO_2$-CuS (blue) as opposed to the Au@$SiO_2$ alone.

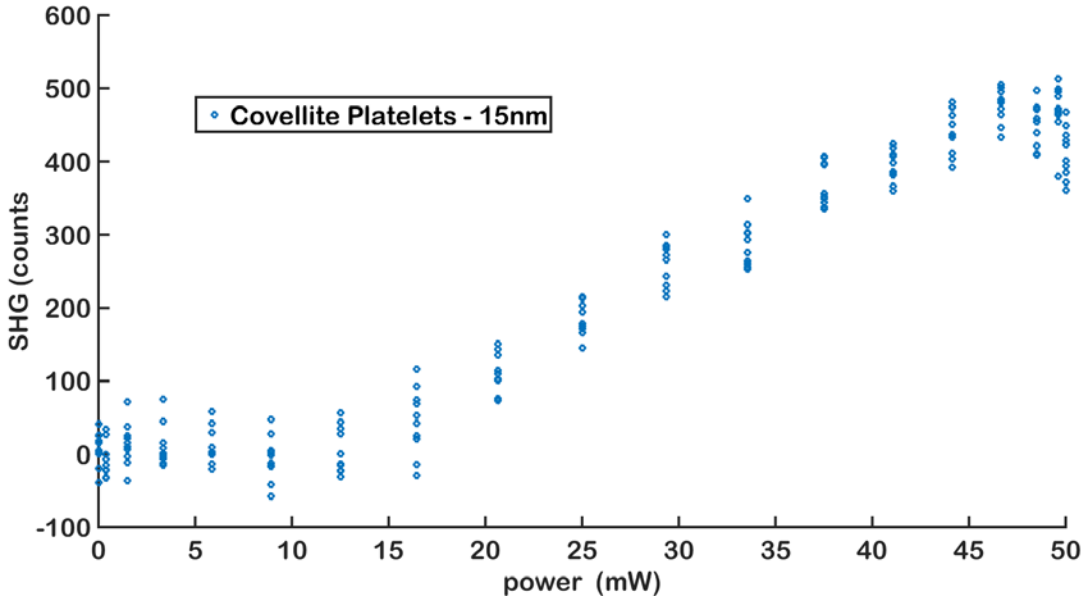


**Figure 23** SHG versus power for CuS platelets alone.

## Appendix C

## Supporting Information for Chapter III, Synthesis of $Au_2S$

### 1) Complete synthetic detail

**$Cu_2S$**

Copper thiolate was prepared by adding (Copper (II) nitrate(0.9mmol), tetraoctylammonium bromide (TOAB)(0.3 mmol), $H_2O$ (32 mL), and $CHCl_3$ (25 mL) to a flask, covering, ad vigorously stirring for twenty minutes. At this point, 240 μL dodecanethiol was added, and the mixture was stirred for an additional twenty minutes. The water layer was poured off, and the $CHCl_3$ was evaporated, leaving a white waxy material which was the copper thiolate. The thiolate was heated in an open 5 dram glass vial in an oil bath for 2.5 hours. To achieve large hexagonal platelets, 50-200nm in diameter, the bath temperature was kept at 200˚C and the reaction was not stirred. To achieve smaller platelets, the reaction was stirred and the oil bath was maintained at around 165-185 ˚C, with lower temperatures yielding smaller particles. The product was collected via centrifugation with methanol followed by redispersion in $CHCl_3$. UV-VIS, TEM, and XRD were used to characterize the product.

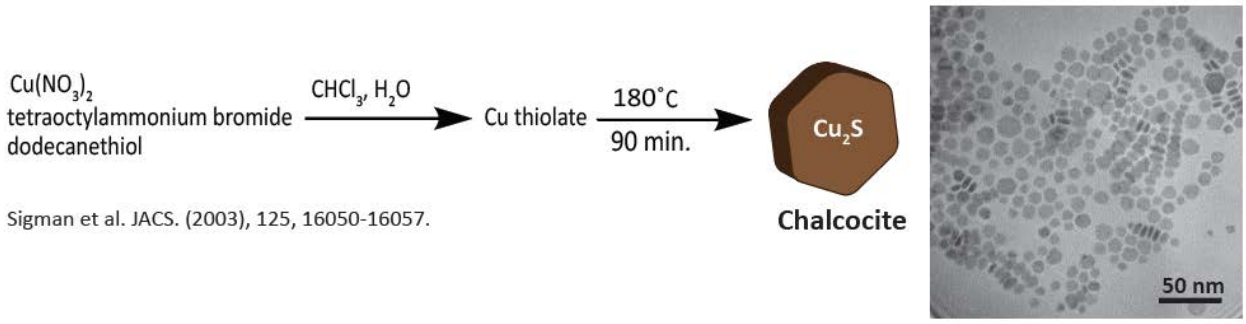


**Figure 24** Copper sulfide synthesis

**$Au_2S$**

A batch of $Cu_2S$ was added to 1 mL oleylamine in a 20 mL 3-neck RB flask and placed under vacuum on a Schlenck line until the solvent was removed. The flask was then flushed with nitrogen and then put under vacuum several more times to remove any dissolved gases. 4-19 mL toluene was then added under nitrogen (less toluene resulted in greater degree of cation exchange). An Au precursor consisting of gold (III) chloride (0.03mmol), dodecylamine(0.2 mmol) didodecyldimethylammonium bromide (DDAB)(0.15 mmol), and toluene was added dropwise to the $Cu_2S$ with vigorous stirring over the course of 3 min, and the reaction continued stirring for 5 minutes after the addition. The product was collected through the addition of methanol and centrifugation at 8000 rpm for 10 min, then washed 2 more times with toluene/MeOH. Product was characterized through UV-Vis, TEM, XRD, XPS.

## 2) Additional characterization

**TEM-induced Au reduction**

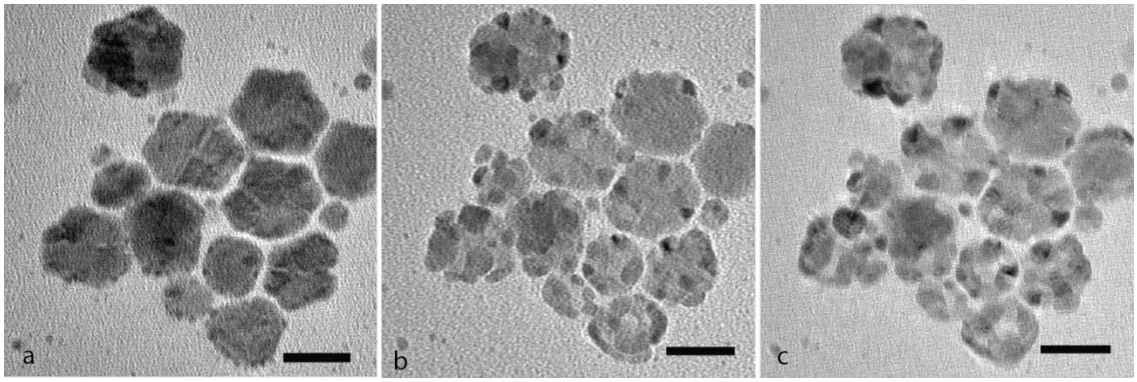


**Figure 25** Series of TEM images of the same particles showing the rapid reduction to metallic Au that occurs on $Au_2S$ particles with smaller (<20 nm) domain sizes of $Au_2S$. FFT analysis of higher-contrast domains that within five minutes of initial image (a) to (c) confirms that these areas are crystalline gold, while lower-contrast regions are $Au_2S$. Nucleation of gold domains occurs at surfaces and domain interfaces('seams') of the gold sulfide crystals, and domain appear to undergo an Ostwald ripening process with continued exposure to the TEM beam, with initial small nucleation points quickly coalescing into a few larger gold domains. Scale bars=20 nm

## TEM of $Cu_2S$ platelets

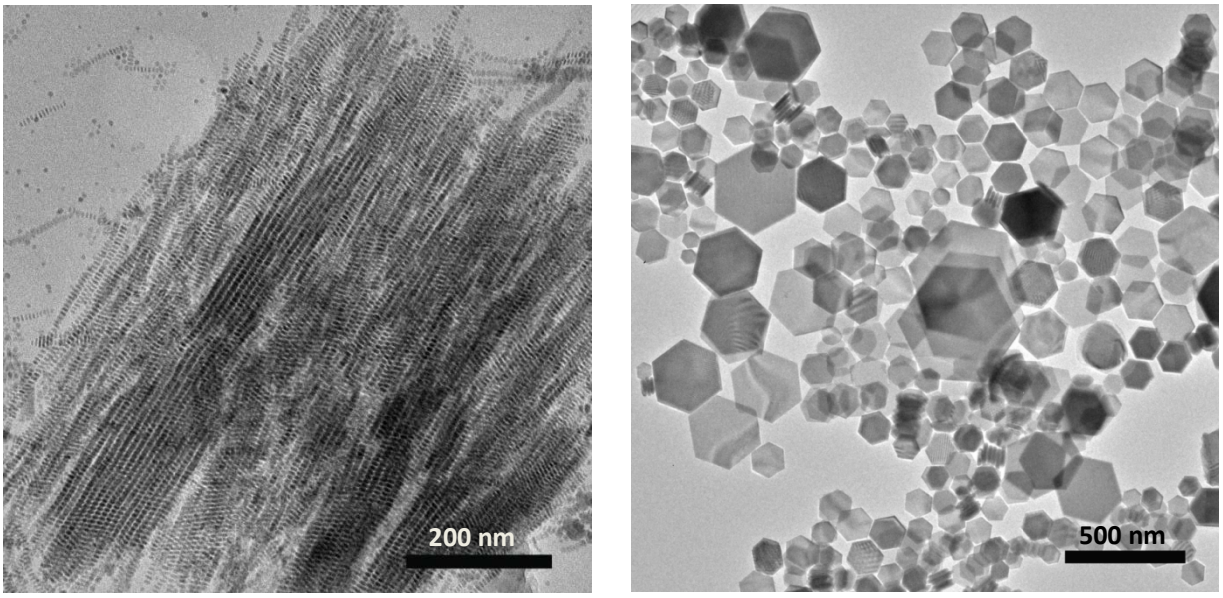


**Figure 26** LR TEM of smaller and larger $Cu_2S$ platelets

## $Au_2S$ STEM-EDS Line Scan

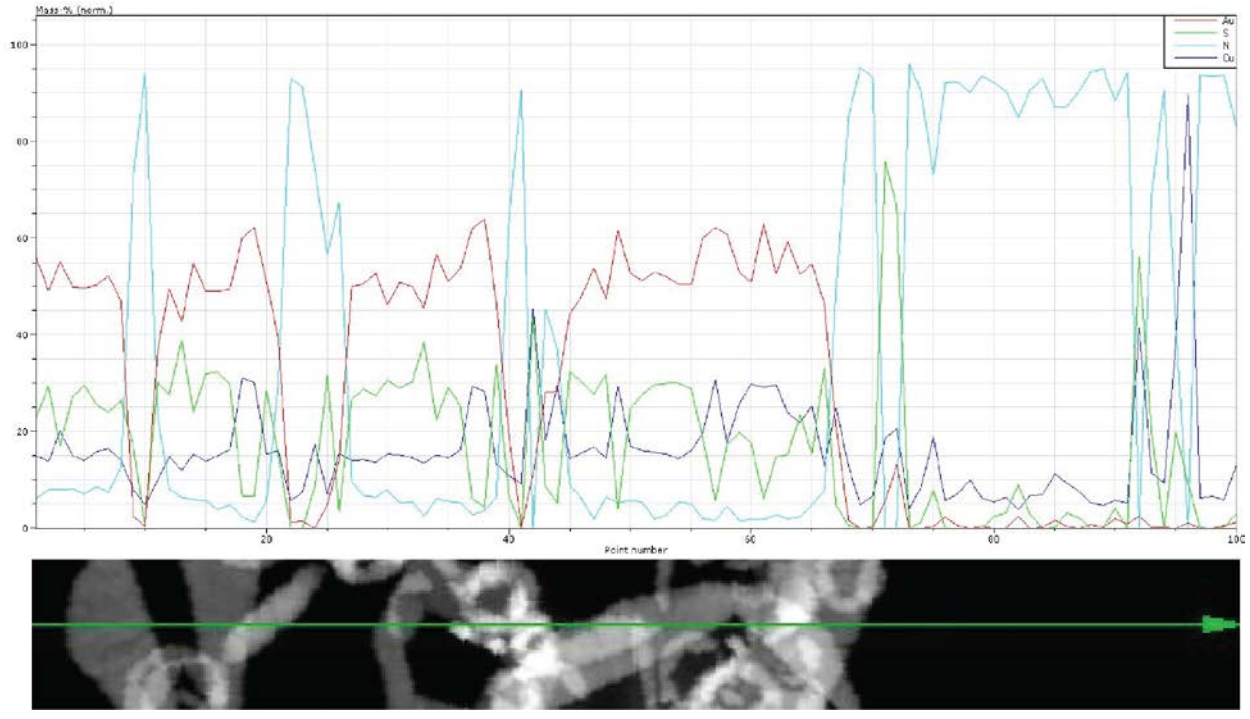


Line-scan STEM-EDS of $Au_2S$ rings showing 2:1 Au:S ratio within ring structures. High Cu background levels are due to the instrument and sample holder.

### 3) Precursor reduction

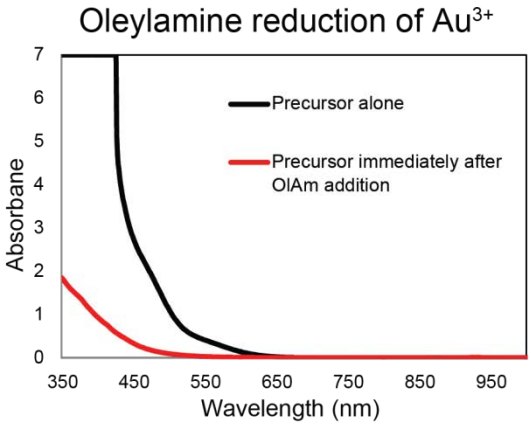


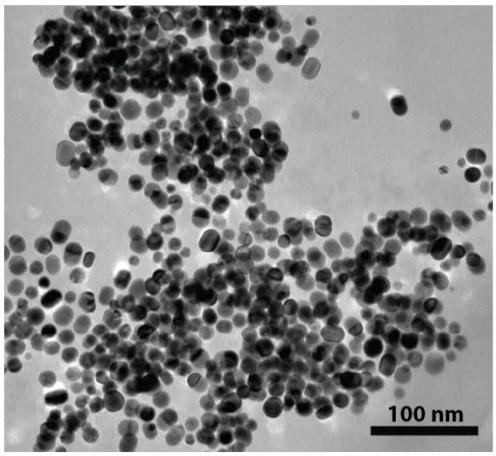


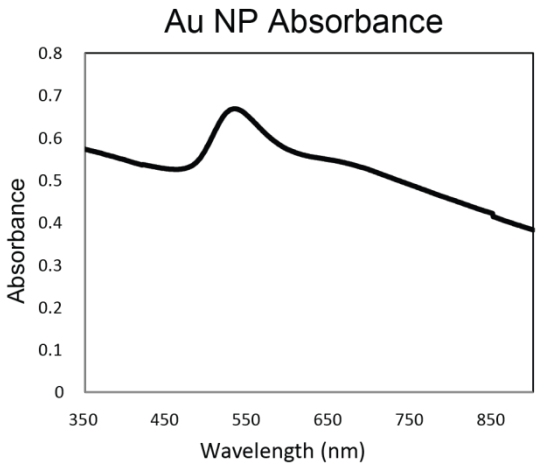


**Figure 25**. UV-Vis of undiluted Au precursor solution shows strong absorption characteristic of an $Au^{3+}$ solution. Upon addition of oleylamine to cuvette, this absorption is instantaneously diminished. After continuous stirring at room temperature for >1 week, the precursor solution turned light pink, indicating the formation of Au NPs. The presence of Au NPs was confirmed by UV-Vis (LSPR peak centered at 530nm) and TEM.

### 4) Thermodynamic Calculations

Following a calculation made by Kundu et al[95]. and the guidelines for estimation set down in Rivest et al.[88] the thermodynamic driving force for this cation exchange was estimated. All values are taken from the CRC handbook. $\Delta H_f^\circ$ is used for the enthalpy of formation of AuCl as $\Delta G_f^\circ$ was not available.

$$2AuCl + Cu_2S \rightarrow Au_2S + 2\,CuCl$$

$$AuCl \rightarrow Au^+ + Cl^- \qquad 2(+34.7)\ \Delta H_f^\circ$$

$$Cu_2S \rightarrow 2Cu+ + S^{2-} \qquad +86.2$$

$$2Au^+ + S^{2-} \rightarrow Au_2S \qquad (+10.8)\ \Delta G_f^\circ$$

$$\underline{2Cu^+ + 2Cl^- \rightarrow 2CuCl} \qquad \underline{2(-119.9)}$$

$$2AuCl + Cu_2S \rightarrow Au_2S + 2CuCl \qquad -73.4\ \Delta G^\circ\ kJ/mol$$

Negative $\Delta G^\circ$ so the exchange should proceed spontaneously.

**5) XPS**

Nanoparticles were dropcast in a toluene solution onto a silicon wafer. XPS was taken a Physical Electronics (PHI) VersaProbe 5000. with Al Kα X-rays (1486.6 eV), a takeoff angle of 45˚, and a spot size of 100 μm. Peaks were fitted using CasaXPS software and were calibrated to the lowest energy C 1s peak at 284.8 eV. Au 4f peaks are consistent with Au(0), as noted in the text. Cu 2p peaks are consistent with $Cu_2S$ as reported by Turo et al.[104] However, the S 2p peaks are not consistent with $S^{1-}$ as would be expected. Fitting only to $S^{1-}$ yielded a poor fit, which was much improved by adding a second fit representing a slightly higher binding energy, centered near 162.4 eV for the S $2p_{3/2}$, which is closer to the binding energy for thiols bound to gold[105] than to the $Cu_2S$ S $2p_{3/2}$ binding energy which falls around 161.8 eV.[106] Although XPS has been noted to be a poor characterization technique[80] for $Au_2S$, this suggests a slight material change and perhaps some Au-S bonding.

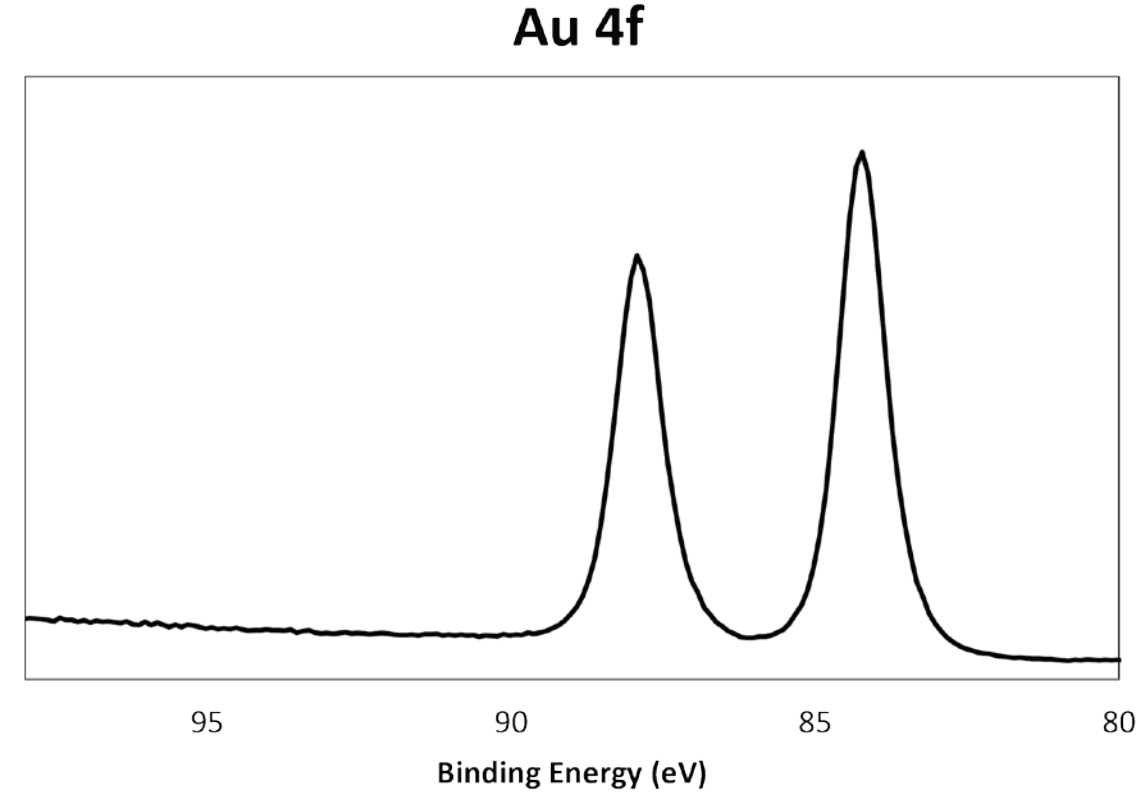
Au 4f
95
90
85
80
Binding Energy (eV)

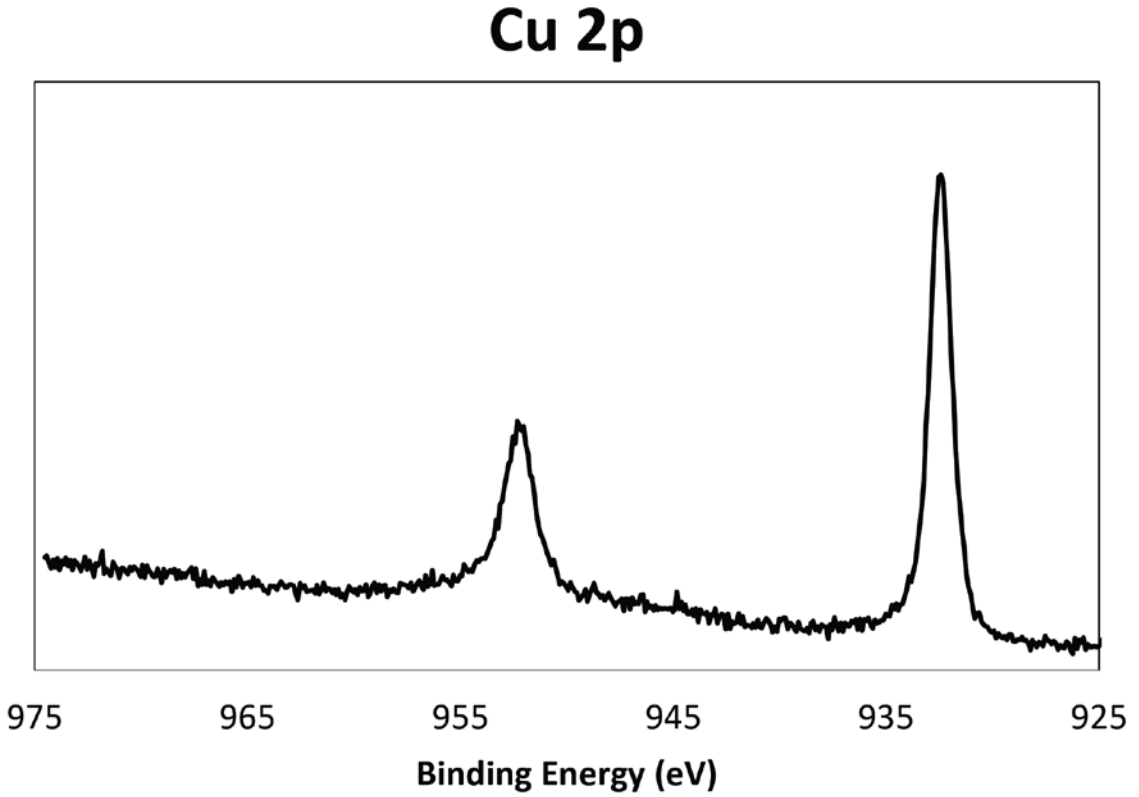
Cu 2p
975
965
955
945
935
925
Binding Energy (eV)

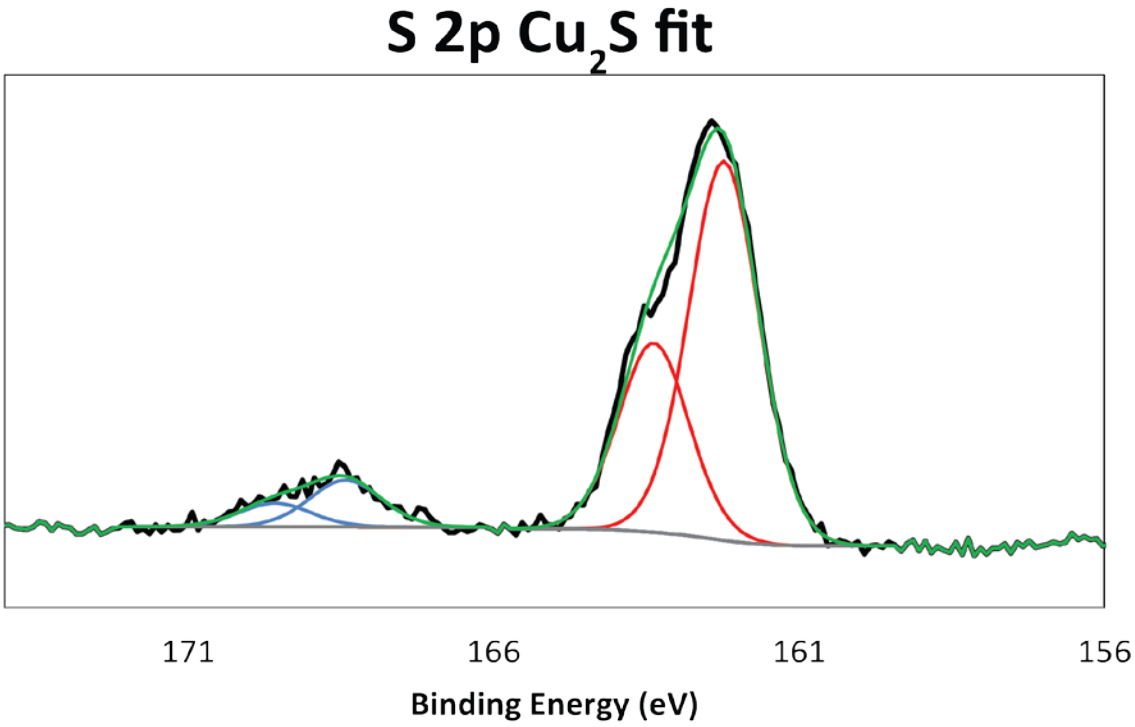


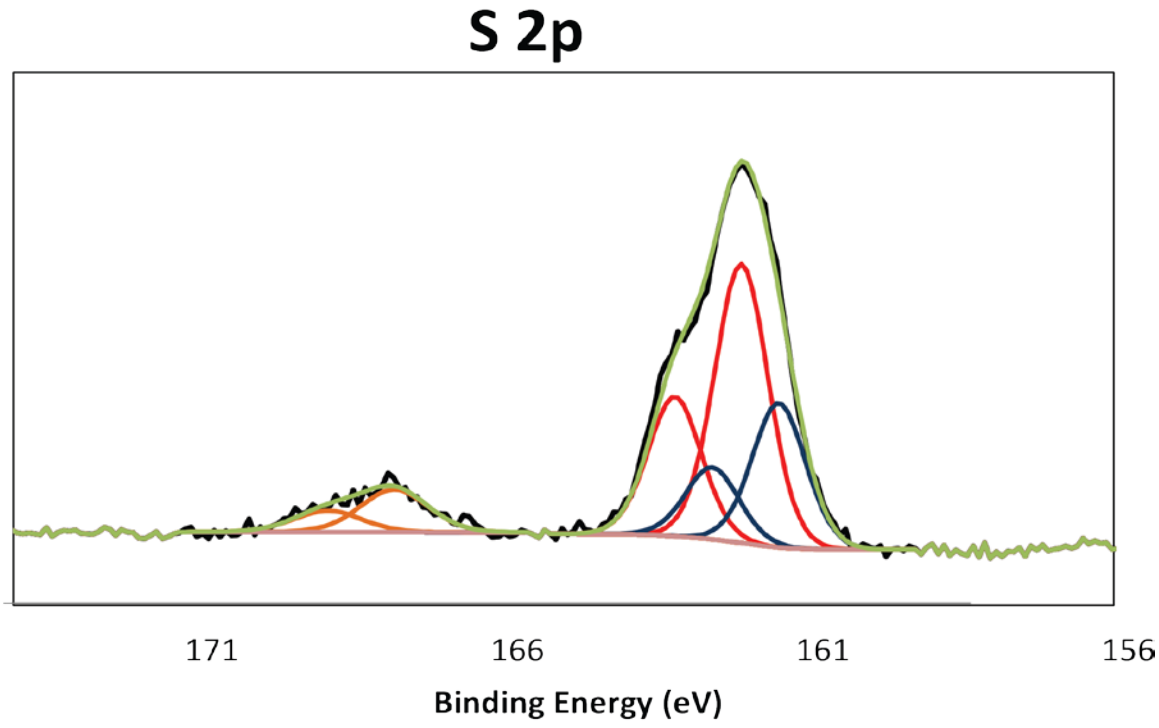


**Figure 27** S 2p XRD peaksTop: S 2p peaks fit as if there were only $Cu_2S$ present. Bottom: S 2p peaks fit with another set of higher energy fits.

## REFERENCES


(1) Shaviv, E.; Del Fatti, N.; Schubert, O.; Alves-Santos, M.; Goldoni, G.; Di Felice, R.; Valle, F.; Banin, U.; Sonnichsen, C. Absorption Properties of Metal- Semiconductor Hybrid Nanoparticles. *ACS Nano* **2011**, *5*, 4712–4719.

(2) Chang, J.; Waclawik, E. R. Colloidal Semiconductor Nanocrystals : Controlled Synthesis and Surface Chemistry in Organic Media. *RSC Adv.* **2014**, *4*, 23505–23527.

(3) You, H.; Yang, S.; Ding, B.; Yang, H. Synthesis of Colloidal Metal and Metal Alloy Nanoparticles for Electrochemical Energy Applications. *Chem. Soc. Rev.* **2013**, *42*, 2880–2904.

(4) Bigall, N. C.; Parak, W. J.; Dorfs, D. Fluorescent, Magnetic and plasmonic—Hybrid Multifunctional Colloidal Nano Objects. *Nano Today* **2012**, *7*, 282–296.

(5) Costi, R.; Saunders, A. E.; Banin, U. Colloidal Hybrid Nanostructures: A New Type of Functional Materials. *Angew. Chem. Int. Ed. Engl.* **2010**, *49*, 4878–4897.

(6) Banin, U.; Ben-Shahar, Y.; Vinokurov, K. Hybrid Semiconductor-Metal Nanoparticles: From Architecture to Function. *Chem. Mater.* **2014**, *26*, 97–110.

(7) Kalisman, P.; Nakibli, Y.; Amirav, L. Perfect Photon-to-Hydrogen Conversion Efficiency. *Nano Lett.* **2016**, *16*, 1776–1781.

(8) Liz-Marzán, L. M.; Giersig, M.; Mulvaney, P. Synthesis of Nanosized Gold−Silica Core−Shell Particles. *Langmuir* **1996**, *12*, 4329–4335.

(9) Dethlefsen, J. R.; Døssing, A. Preparation of a ZnS Shell on CdSe Quantum Dots Using a Single-Molecular ZnS Precursor. *Nano Lett.* **2011**, *11*, 1964–1969.

(10) Cortie, M. B.; McDonagh, A. M. Synthesis and Optical Properties of Hybrid and Alloy Plasmonic Nanoparticles. *Chem. Rev.* **2011**, *111*, 3713–3735.

(11) Khon, E.; Mereshchenko, A.; Tarnovsky, A. N.; Acharya, K.; Klinkova, A.; Hewa-Kasakarage, N. N.; Nemitz, I.; Zamkov, M. Suppression of the Plasmon Resonance in Au/CdS Colloidal Nanocomposites. *Nano Lett.* **2011**, *11*, 1792–1799.

(12) Wang, C.; Yin, H.; Dai, S.; Sun, S. A General Approach to Noble Metal−Metal Oxide Dumbbell Nanoparticles and Their Catalytic Application for CO Oxidation. *Chem. Mater.* **2010**, *22*, 3277–3282.

(13) Kelly, K. L.; Kelly, K. L.; Coronado, E.; Zhao, L.; Coronado, E.; Schatz, G. C.; Zhao, L. L.; Schatz, G. C. The Optical Properties of Metal Nanoparticles: The Influence of Size, Shape, and Dielectric Environment. *J. Phys. Chem. B* **2003**, *107*, 668–677.

(14) Zhang, J. Z.; Noguez, C. Plasmonic Optical Properties and Applications of Metal Nanostructures. *Plasmonics* **2008**, *3*, 127–150.

(15) Garcia, M. a. Surface Plasmons in Metallic Nanoparticles: Fundamentals and Applications.

*J. Phys. D. Appl. Phys.* **2012**, *45*, 389501.

(16) Niezgoda, J.; Harrison, M. Novel Synthesis of Chalcopyrite $Cu_xIn_yS_2$ Quantum Dots with Tunable Localized Surface Plasmon Resonances. *Chem. Mater.* **2012**, *24*, 3294–3298.

(17) Naik, G. V; Shalaev, V. M.; Boltasseva, A. Alternative Plasmonic Materials: Beyond Gold and Silver. *Adv. Mater.* **2013**, *25*, 3264–3294.

(18) Riha, S. C.; Johnson, D. C.; Prieto, A. L. Cu2Se Nanoparticles with Tunable Electronic Properties due to a Controlled Solid-State Phase Transition Driven by Copper Oxidation and Cationic Conduction. *J. Am. Chem. Soc.* **2011**, *133*, 1383–1390.

(19) Xie, Y.; Riedinger, A.; Prato, M.; Casu, A.; Genovese, A.; Guardia, P.; Sottini, S.; Sangregorio, C.; Miszta, K.; Ghosh, S.; *et al.* Copper Sulfide Nanocrystals with Tunable Composition by Reduction of Covellite Nanocrystals with Cu+ Ions. *J. Am. Chem. Soc.* **2013**, *135*, 17630–17637.

(20) Luther, J. M.; Jain, P. K.; Ewers, T.; Alivisatos, A. P. Localized Surface Plasmon Resonances Arising from Free Carriers in Doped Quantum Dots. *Nat. Mater.* **2011**, *10*, 361–366.

(21) Jain, P. K.; Luther, J.; Ewers, T.; Alivisatos, A. P. Near-Infrared Localized Surface Plasmon Resonances Arising from Free Carriers in Doped Quantum Dots. *Nat. Mater.* **2010**, *10*, 361–366.

(22) Comin, A.; Manna, L. New Materials for Tunable Plasmonic Colloidal Nanocrystals. *Chem. Soc. Rev.* **2014**, *43*, 3957–3975.

(23) Sperling, R.; Gil, P.; Zhang, F. Biological Applications of Gold Nanoparticles. *Chem. Soc. Rev.* **2008**, *37*, 1896–1908.

(24) Dreaden, E. C.; Alkilany, A. M.; Huang, X.; Murphy, C. J.; El-Sayed, M. A. The Golden Age: Gold Nanoparticles for Biomedicine. *Chem. Soc. Rev.* **2012**, *41*, 2740–2779.

(25) Wu, H.-L.; Tsai, H.-R.; Hung, Y.-T.; Lao, K.-U.; Liao, C.-W.; Chung, P.-J.; Huang, J.-S.; Chen, I.-C.; Huang, M. H. A Comparative Study of Gold Nanocubes, Octahedra, and Rhombic Dodecahedra as Highly Sensitive SERS Substrates. *Inorg. Chem.* **2011**, *50*, 8106–8111.

(26) Lin, H. Y.; Chen, Y. F.; Wu, J. G.; Wang, D. I.; Chen, C. C. Carrier Transfer Induced Photoluminescence Change in Metal-Semiconductor Core-Shell Nanostructures. *Appl. Phys. Lett.* **2006**, *88*, 57–60.

(27) Ma, X.; Fletcher, K.; Kipp, T. Photoluminescence of Individual Au/CdSe Nanocrystal Complexes with Variable Interparticle Distances. *J. Phys. Chem. Lett.* **2011**, *2*, 2466–2471.

(28) Boyde, R. W. *Nonlinear Optics, Third Edition*; 2008.

(29) Levenson, M.; Kano, S. *Introduction to Nonlinear Laser Spectroscopy: Revised Edition*; 1988.

(30) Zernike, F.; Midwinter, J. E. *Applied Nonlinear Optics*; 1973.

(31) Kauranen, M.; Zayats, A. V. Nonlinear Plasmonics. *Nat. Photonics* **2012**, *6*, 737–748.

(32) Jais, P.; von Bilderling, C.; Bragas, A. Plasmon-Enhanced Second Harmonic Generation in Semiconductor Quantum Dots close to Metal Nanoparticles. *Pap. Phys.* **2011**, *3*, 030002.

(33) Singh, M. Enhancement of the Second-Harmonic Generation in a Quantum Dot-Metallic Nanoparticle Hybrid System. *Nanotechnology* **2013**, *24*, 125701.

(34) Slablab, A.; Le Xuan, L.; Zielinski, M.; de Wilde, Y.; Jacques, V.; Chauvat, D.; Roch, J.-F. Second-Harmonic Generation from Coupled Plasmon Modes in a Single Dimer of Gold Nanospheres. *Opt. Express* **2012**, *20*, 220–227.

(35) Shaviv, E.; Banin, U. Synergistic Effects on Second Harmonic Generation of Hybrid CdSe-Au Nanoparticles. *ACS Nano* **2010**, *4*, 1529–1538.

(36) Faucheaux, J. A.; Stanton, A. L. D.; Jain, P. K. Plasmon Resonances of Semiconductor Nanocrystals: Physical Principles and New Opportunities. *J. Phys. Chem. Lett.* **2014**, *5*, 976–985.

(37) Xie, Y.; Carbone, L.; Nobile, C.; Grillo, V.; Agostino, S. D.; Sala, F. Della; Giannini, C.; Altamura, D.; Oelsner, C.; Kryschi, X. C.; *et al.* Metallic-like Stoichiometric Copper Sulfide Nanocrystals: Phase- and Shape-Selective Synthesis, Near-Infrared Surface Plasmon Resonance Properties , and Their Modeling. *ACS Nano* **2013**, *7*, 7352–7369.

(38) Du, W.; Qian, X.; Xiaodong, M.; Gong, Q.; Cao, H.; Yin, J. Shape-Controlled Synthesis and Self-Assembly of Hexagonal Covellite (CuS) Nanoplatelets. *Chem. - A Eur. J.* **2007**, *13*, 3241–3247.

(39) Moreira, D. P. R.; Alemany, P.; Canadell, E. Nature of Holes, Oxidation States, and Hypervalency in Covellite (CuS). *Inorg. Chem.* **2014**, *53*, 12402–12406.

(40) Goh, S. W.; Buckley, A. N.; Lamb, R. N. Copper(II) Sulfide? *Miner. Eng.* **2006**, *19*, 204–208.

(41) Tian, X. R.; Tong, L. M.; Xu, H. X. New Progress of Plasmonics in Complex Metal Nanostructures. *Sci. China Physics, Mech. Astron.* **2013**, *56*, 2327–2336.

(42) Zohar, N.; Chuntonov, L.; Haran, G. The Simplest Plasmonic Molecules: Metal Nanoparticle Dimers and Trimers. *J. Photochem. Photobiol. C Photochem. Rev.* **2014**, *21*, 26–39.

(43) Ding, X.; Liow, C. H.; Zhang, M.; Huang, R.; Li, C.; Shen, H.; Liu, M.; Zou, Y.; Gao, N.; Zhang, Z.; *et al.* Surface Plasmon Resonance Enhanced Light Absorption and Photothermal Therapy in the Second near-Infrared Window. *J. Am. Chem. Soc.* **2014**, *136*, 15684–15693.

(44) Liu, X.; Lee, C.; Law, W.; Zhu, D.; Liu, M.; Jeon, M.; Kim, J.; Prasad, P. N.; Kim, C.;

Swihart, M. T. Au-$Cu_{2-x}Se$ Heterodimer Nanoparticles with Broad Localized Surface Plasmon Resonance as Contrast Agents for Deep Tissue Imaging. *Nano Lett.* **2013**.

(45) Mokari, T.; Sztrum, C. G.; Salant, A.; Rabani, E.; Banin, U. Formation of Asymmetric One-Sided Metal-Tipped Semiconductor Nanocrystal Dots and Rods. *Nat. Mater.* **2005**, *4*, 855–863.

(46) Fu, A.; Micheel, C. M.; Cha, J.; Chang, H.; Yang, H.; Alivisatos, P. Discrete Nanostructures of Quantum Dots / Au with DNA Discrete Nanostructures of Quantum Dots / Au with DNA. **2004**, *126*, 10832–10833.

(47) Govorov, A. O.; Bryant, G. W.; Zhang, W.; Skeini, T.; Lee, J.; Kotov, N. A.; Slocik, J. M.; Naik, R. R. Exciton-Plasmon Interaction and Hybrid Excitons in Semiconductor-Metal Nanoparticle Assemblies. *Nano Lett.* **2006**, *6*, 984–994.

(48) Agarwal, A.; Lilly, G. D.; Govorov, A. O.; Kotov, N. A. Optical Emission and Energy Transfer in Nanoparticle-Nanorod Assemblies: Potential Energy Pump System for Negative Refractive Index Materials. *J. Phys. Chem. C* **2008**, *112*, 18314–18320.

(49) Khanal, B. P.; Pandey, A.; Li, L.; Lin, Q.; Bae, W. K.; Luo, H.; Klimov, V. I.; Pietryga, J. M. Generalized Synthesis of Hybrid Metal-Semiconductor Nanostructures Tunable from the Visible to the Infrared. *ACS Nano* **2012**, *6*, 3832–3840.

(50) Liu, N.; Prall, B. S.; Klimov, V. I. Hybrid Gold/silica/nanocrystal-Quantum-Dot Superstructures: Synthesis and Analysis of Semiconductor-Metal Interactions. *J. Am. Chem. Soc.* **2006**, *128*, 15362–15363.

(51) Hu, Y.; Sun, Y. A Generic Approach for the Synthesis of Dimer Nanoclusters and Asymmetric Nanoassemblies. *J. Am. Chem. Soc.* **2013**, *135*, 2213–2221.

(52) Bahadur, N. M.; Watanabe, S.; Furusawa, T.; Sato, M.; Kurayama, F.; Siddiquey, I. A.; Kobayashi, Y.; Suzuki, N. Rapid One-Step Synthesis, Characterization and Functionalization of Silica Coated Gold Nanoparticles. *Colloids Surfaces A Physicochem. Eng. Asp.* **2011**, *392*, 137–144.

(53) Graf, C.; Vossen, D. L. J.; Imhof, A.; van Blaaderen, A. A General Method To Coat Colloidal Particles with Silica. *Langmuir* **2003**, *19*, 6693–6700.

(54) Jana, N.; Earhart, C.; Ying, J. Synthesis of Water-Soluble and Functionalized Nanoparticles by Silica Coating. *Chem. Mater.* **2007**, 5074–5082.

(55) Wu, Z.; Liang, J.; Ji, X.; Yang, W. Preparation of Uniform Au@$SiO_2$ Particles by Direct Silica Coating on Citrate-Capped Au Nanoparticles. *Colloids Surfaces A Physicochem. Eng. Asp.* **2011**, *392*, 220–224.

(56) Enustun, B. Y. B. V. Coagulation of Colloidal Gold. *J. Am. Chem. Soc.* **1963**, *85*, 3317–3328.

(57) Jana, N. R.; Gearheart, L.; Murphy, C. J. Seeding Growth for Size Control of 5−40 nm Diameter Gold Nanoparticles. *Langmuir* **2001**, *17*, 6782–6786.

(58) Mine, E.; Yamada, A.; Kobayashi, Y.; Konno, M.; Liz-Marzán, L. M. Direct Coating of Gold Nanoparticles with Silica by a Seeded Polymerization Technique. *J. Colloid Interface Sci.* **2003**, *264*, 385–390.

(59) Motl, N. E.; Smith, A. F.; DeSantis, C. J.; Skrabalak, S. E. Engineering Plasmonic Metal Colloids through Composition and Structural Design. *Chem. Soc. Rev.* **2014**, *43*, 3823–3834.

(60) Kobayashi, Y.; Correa-Duarte, M. A.; Liz-Marzan, L. M. Sol-Gel Processing of Silica-Coated Gold Nanoparticles. **2001**, 6375–6379.

(61) Westcott, S.; Oldenburg, S.; Lee, T.; Halas, N. Formation and Adsorption of Clusters of Gold Nanoparticles onto Functionalized Silica Nanoparticle Surfaces. *Langmuir* **1998**, *7463*, 5396–5401.

(62) Hessel, C. M.; Pattani, V. P.; Rasch, M.; Panthani, M. G.; Koo, B.; Tunnell, J. W.; Korgel, B. A. Copper Selenide Nanocrystals for Photothermal Therapy. *Nano Lett.* **2011**, *11*, 2560–2566.

(63) Huang, X.; El-Sayed, M. A. Plasmonic Photo-Thermal Therapy (PPTT). *Alexandria J. Med.* **2011**, *47*, 1–9.

(64) Reineck, P.; Gómez, D.; Ng, S. H.; Karg, M.; Bell, T.; Mulvaney, P.; Bach, U. Distance and Wavelength Dependent Quenching of Molecular Fluorescence by Au@$SiO_2$ Core-Shell Nanoparticles. *ACS Nano* **2013**.

(65) Sowers, K. L.; Swartz, B.; Krauss, T. D. Chemical Mechanisms of Semiconductor Nanocrystal Synthesis. *Chem. Mater.* **2013**, *25*, 1351–1362.

(66) Goel, S.; Chen, F.; Cai, W. Synthesis and Biomedical Applications of Copper Sulfide Nanoparticles: From Sensors to Theranostics. *Small* **2014**, *10*, 631–645.

(67) Zhao, Y.; Burda, C. Development of Plasmonic Semiconductor Nanomaterials with Copper Chalcogenides for a Future with Sustainable Energy Materials. *Energy Environ. Sci.* **2012**, *5*, 5564.

(68) Ramasamy, K.; Malik, M. A.; Revaprasadu, N.; Brien, P. O. Routes to Nanostructured Inorganic Materials with Potential for Solar Energy Applications Routes to Nanostructured Inorganic Materials with Potential for Solar Energy Applications. *Chem. Mater.* **2013**, *25*, 3551–3569.

(69) Wang, D.; Hao, C.; Zheng, W.; Peng, Q.; Wang, T.; Liao, Z.; Yu, D.; Li, Y. Ultralong Single-Crystalline $Ag_2S$ Nanowires: Promising Candidates for Photoswitches and Room-Temperature Oxygen Sensors. *Adv. Mater.* **2008**, *20*, 2628–2632.

(70) Gobin, A. M.; Watkins, E. M.; Quevedo, E.; Colvin, V. L.; West, J. L. Near-Infrared-Resonant Gold/Gold Sulfide Nanoparticles as a Photothermal Cancer Therapeutic Agent. *Small* **2010**, *6*, 745–752.

(71) Kristl, M.; Drofenik, M. Preparation of $Au_2S_3$ and Nanocrystalline Gold by Sonochemical

Method. *Inorg. Chem. Commun.* **2003**, *6*, 1419–1422.

(72) Morris, T.; Copeland, H.; Szulczewski, G. Synthesis and Characterization of Gold Sulfide Nanoparticles. *Langmuir* **2002**, 535–539.

(73) Ishikawa, K.; Isonaga, T.; Wakita, S.; Suzuki, Y. Structure and Electrical Properties of $Au_2S$. *Solid State Ionics* **1995**, *79*, 60–66.

(74) Saunders, A. E.; Popov, I.; Banin, U. Synthesis of Hybrid CdS-Au Colloidal Nanostructures. *J. Phys. Chem. B* **2006**, *110*, 25421–25429.

(75) Schmidbaur, H.; Cronje, S.; Djordjevic, B.; Schuster, O. Understanding Gold Chemistry through Relativity. *Chem. Phys.* **2005**, *311*, 151–161.

(76) Yoshizawa, K.; Iwahori, K.; Sugimoto, K.; Yamashita, I. Fabrication of Gold Sulfide Nanoparticles Using the Protein Cage of Apoferritin. *Chem. Lett.* **2006**, *35*, 1192–1193.

(77) Bacinello, D.; Durand, E.; Valle, F.; Tre, M.; Uni, V.; Schweitzer, V.; Cedex, P.; No, V. Synthesis of Hybrid Gold - Gold Sulfide Colloidal Particles. *Langmuir* **2008**, 4289–4294.

(78) Chatterjee, K.; Basu, S.; Chakravorty, D. Plasmon Resonance Absorption in Sulfide-Coated Gold Nanorods. *J. Mater. Res.* **2006**, *21*, 34–40.

(79) Kuo, C.; Huang, M. H. Hydrothermal Synthesis of Free-Floating $Au_2S$ Nanoparticle Superstructures. *J. Phys. Chem. C.* **2008**, *112*, 11661–11666.

(80) Mikhlin, Y.; Likhatski, M.; Tomashevich, Y.; Romanchenko, A.; Erenburg, S.; Trubina, S. XAS and XPS Examination of the Au–S Nanostructures Produced via the Reduction of Aqueous gold(III) by Sulfide Ions. *J. Electron Spectros. Relat. Phenomena* **2010**, *177*, 24–29.

(81) Okamoto, H.; Massalski, T. B. The Gold-Sulfur System. *Bull. Alloy phase diagrams* **1985**, *6*, 518–519.

(82) Averitt, R.; Sarkar, D.; Halas, N. Plasmon Resonance Shifts of Au-Coated $Au_2S$ Nanoshells: Insight into Multicomponent Nanoparticle Growth. *Phys. Rev. Lett.* **1997**, *78*, 4217–4220.

(83) Schwartzberg, A. M.; Grant, C. D.; van Buuren, T.; Zhang, J. Z. Reduction of $HAuCl_4$ by $Na_2S$ Revisited: The Case for Au Nanoparticle Aggregates and against $Au_2S$/Au Core/Shell Particles. *J. Phys. Chem. C* **2007**, *111*, 8892–8901.

(84) Young, J. K.; Figueroa, E. R.; Drezek, R. A. Tunable Nanostructures as Photothermal Theranostic Agents. *Ann. Biomed. Eng.* **2012**, *40*, 438–459.

(85) Huang, H.; Liu, X.; Zeng, Y.; Yu, X.; Liao, B.; Yi, P.; Chu, P. K. Optical and Biological Sensing Capabilities of $Au_2S$/AuAgS Coated Gold Nanorods. *Biomaterials* **2009**, *30*, 5622–5630.

(86) Wang, X.; Liu, X.; Zhu, D.; Swihart, M. T. Controllable Conversion of Plasmonic $Cu_{2-x}S$ Nanoparticles to $Au_2S$ by Cation Exchange and Electron Beam Induced Transformation of

$Cu_{2-x}S$-$Au_2S$ Core/shell Nanostructures. *Nanoscale* **2014**, *6*, 8852–8857.

(87) van der Stam, W.; Bladt, E.; Rabouw, F. T.; Bals, S.; de Mello Donega, C. Near-Infrared Emitting $CuInSe_2$/CuInS Dot Core/Rod Shell Heteronanorods by Sequential Cation Exchange. *ACS Nano* **2015**, *9*, 11430–11438.

(88) Rivest, J. B.; Jain, P. K. Cation Exchange on the Nanoscale: An Emerging Technique for New Material Synthesis, Device Fabrication, and Chemical Sensing. *Chem. Soc. Rev.* **2013**, 89–96.

(89) Son, D. H.; Hughes, S. M.; Yin, Y.; Paul Alivisatos, A. Cation Exchange Reactions in Ionic Nanocrystals. *Science* **2004**, *306*, 1009–1012.

(90) Moon, G. D.; Ko, S.; Min, Y.; Zeng, J.; Xia, Y.; Jeong, U. Chemical Transformations of Nanostructured Materials. *Nano Today* **2011**, *6*, 186–203.

(91) Beberwyck, B. J.; Surendranath, Y.; Alivisatos, A. P. Cation Exchange: A Versatile Tool for Nanomaterials Synthesis. *J. Phys. Chem. C* **2013**, *117*, 19759–19770.

(92) Buck, M. R.; Schaak, R. E. Emerging Strategies for the Total Synthesis of Inorganic Nanostructures. *Angew. Chemie - Int. Ed.* **2013**, *52*, 6154–6178.

(93) Rivest, J. B.; Jain, P. K. Cation Exchange on the Nanoscale: An Emerging Technique for New Material Synthesis, Device Fabrication, and Chemical Sensing. *Chem. Soc. Rev.* **2013**, 89–96.

(94) Gupta, S.; Kershaw, S. V.; Rogach, A. L. 25th Anniversary Article: Ion Exchange in Colloidal Nanocrystals. *Adv. Mater.* **2013**, *25*, 6923–6944.

(95) Kundu, S.; Kundu, P.; Tendeloo, G. Van; Ravishankar, N. $Au_2S_x$/CdS Nanorods by Cation Exchange: Mechanistic Insights into the Competition between Cation-Exchange and Metal Ion Reduction. *Small* **2014**, 3895–3900.

(96) Yoon, D.; Jin, H.; Ryu, S.; Park, S.; Baik, H.; Oh, S. J.; Haam, S.; Joo, C.; Lee, K. Scalable Synthesis of Djurleite Copper Sulphide ($Cu_{1.94}S$) Hexagonal Nanoplates from a Single Precursor Copper Thiocyanate and Their Photothermal Properties. *CrystEngComm* **2015**, *17*, 4627–4631.

(97) Sigman, M. B.; Ghezelbash, A.; Hanrath, T.; Saunders, A. E.; Lee, F.; Korgel, B. A. Solventless Synthesis of Monodisperse $Cu_2S$ Nanorods , Nanodisks , and Nanoplatelets. **2003**, 16050–16057.

(98) Macdonald, J. E.; Bar Sadan, M.; Houben, L.; Popov, I.; Banin, U. Hybrid Nanoscale Inorganic Cages. *Nat. Mater.* **2010**, *9*, 810–815.

(99) Ionic Radii in Crystals. In *CRC Handbook of Chemistry and Physics*; Vol. 96, pp. 12–11.

(100) Toledano, P.; Dmitriev, V. *Reconstructive Phase Transitions: In Crystals and Quasicrystals*.

(101) Oh, A.; Baik, H.; Choi, D. S.; Cheon, J. Y.; Kim, B.; Kim, H.; Kwon, S. J.; Joo, S. H.;

Jung, Y.; Lee, K. Skeletal Octahedral Nanoframe with Cartesian Coordinates via Geometrically Precise Nanoscale Phase Segregation in a Pt@Ni Core-Shell Nanocrystal. *ACS Nano* **2015**, *9*, 2856–2867.

(102) Database of Electron Inelastic Mean Free Path for Elemental Solids. *Natl. Inst. Mater. Sci. Japan* **2011**, 1–21.

(103) Kim, Y.; Park, K. Y.; Jang, D. M.; Song, Y. M.; Kim, H. S.; Cho, Y. J.; Myung, Y.; Park, J. Synthesis of Au - $Cu_2S$ Core - Shell Nanocrystals and Their Photocatalytic and Electrocatalytic Activity. *J. Phys. Chem. C.* **2010**, *114*, 22141–22146.

(104) Turo, M. J.; Macdonald, J. E. Crystal-Bound vs Surface-Bound Thiols on Nanocrystals. *ACS Nano* **2014**, *8*, 10205–10213.

(105) Gobbo, P.; Biesinger, M. C.; Workentin, M. S. Facile Synthesis of Gold Nanoparticle (AuNP)–Carbon Nanotube (CNT) Hybrids through an Interfacial Michael Addition Reaction. *Chem. Commun.* **2013**, *49*, 2831.

(106) Biesinger, M. C.; Hart, B. R.; Polack, R.; Kobe, B. A.; Smart, R. S. C. Analysis of Mineral Surface Chemistry in Flotation Separation Using Imaging XPS. *Miner. Eng.* **2007**, *20*, 152–162.